



---

Applied Computational  
Electromagnetics Society

---



Newsletter  
Volume 20 – No. 3  
ISSN 1056-9170



November 2005



# APPLIED COMPUTATIONAL ELECTROMAGNETICS SOCIETY (ACES)

## NEWSLETTER

Vol. 20 No. 3

November 2005

### TABLE OF CONTENTS

<b>COMMITTEE REPORTS</b>	
Election Committee Report .....	7
<b>PERSPECTIVES IN CEM</b>	
“New Modelling Army” Alistair Duffy .....	8
<b>THE PRATICAL CEMist</b>	
“HF Fractal Wire Antenna Case Study” W. Perry Wheless, Michael A. McNees .....	11
<b>TECHNICAL FEATURE ARTICLE</b>	
“The Computational Electromagnetic Framework” Edgar L. Coffey .....	17
<b>TUTORIAL</b>	
“Surface-Based Integral Equation Formulations for Multiple Material and Conducting Objects” Vikram Jandhyala and Swagato Chakraborty .....	25
<b>APPLICATION ARTICLE</b>	
“A Broadband Double Ridge Guise Horn with Improved Radiation Pattern” Vicente Rodriguez .....	48
<b>CALL FOR PAPERS</b>	
The 22 <sup>nd</sup> International Review of Progress in Applied Computational Electromagnetics (ACES 2006) .....	60
<b>ANNOUNCEMENTS:</b>	
ADVERTISING Rates .....	62
DEADLINE for Submission of Articles.....	62
Last Word .....	62

<b>PERMANENT STANDING COMMITTEES OF ACES, INC.</b>
--

<b>COMMITTEE</b>	<b>CHAIRMAN</b>	<b>ADDRESS</b>
NOMINATION	Rene Allard	Penn State University PO Box 30 State College, PA 16804-0030 <a href="mailto:rja5@psu.edu">rja5@psu.edu</a>
ELECTIONS	Rene Allard	Penn State University PO Box 30 State College, PA 16804-0030 <a href="mailto:rja5@psu.edu">rja5@psu.edu</a>
FINANCE	Andrew Peterson	Georgia Institute of Technology School of ECE Atlanta, GA 30332-0250 <a href="mailto:peterson@ece.gatech.edu">peterson@ece.gatech.edu</a>
PUBLICATIONS	Atef Elsherbeni	EE Department, Anderson Hall University of Mississippi University, MS 38677 <a href="mailto:atef@olemiss.edu">atef@olemiss.edu</a>
CONFERENCE	Osama Mohammed	Florida International University ECE Department Miami, FL 33174 <a href="mailto:mohammed@fiu.edu">mohammed@fiu.edu</a>
AWARDS	Ray Perez	Martin Marietta Astronautics MS 58700, PO Box 179 Denver, CO 80201 <a href="mailto:ray.j.perez@lmco.com">ray.j.perez@lmco.com</a>

<b>MEMBERSHIP ACTIVITY COMMITTEES OF ACES, INC.</b>
---

<b>COMMITTEE</b>	<b>CHAIRMAN</b>	<b>ADDRESS</b>
SOFTWARE VALIDATION	Bruce Archambeault	IBM 3039 Cornwallis Road, PO Box 12195 Dept. 18DA B306 Research Triangle Park NC 27709
HISTORICAL	(Vacant)	
CONSTITUTION & BYLAWS	Leo Kempel	2120 Engineering Building Michigan State University East Lansing, MI 48824 <a href="mailto:kempel@egr.msu.edu">kempel@egr.msu.edu</a>
MEMBERSHIP & COMMUNICATIONS	Vicente Rodriguez	ETS-LINDGREN L.P. 1301 Arrow Point Drive Cedar Park, TX 78613 <a href="mailto:rodriguez@ieee.org">rodriguez@ieee.org</a>
INDUSTRIAL RELATIONS	Andy Drodz	ANDRO Consulting Services PO Box 543 Rome, NY 13442-0543 <a href="mailto:Andro1@aol.com">Andro1@aol.com</a>

## ACES NEWSLETTER STAFF

### EDITOR-IN-CHIEF, NEWSLETTER

Bruce Archambeault  
IBM  
3039 Cornwallis Road, PO Box 12195  
Dept. 18DA B306  
Research Triangle Park, NC 27709  
Phone: 919-486-0120  
email: [barch@us.ibm.com](mailto:barch@us.ibm.com)

### EDITOR-IN-CHIEF, PUBLICATIONS

Atef Elsherbeni  
EE Department, Anderson Hall  
University of Mississippi  
University, MS 38677  
Email: [atef@olemiss.edu](mailto:atef@olemiss.edu)

### ASSOCIATE EDITOR-IN-CHIEF

Ray Perez  
Martin Marietta Astronautics  
MS 58700, PO Box 179  
Denver, CO 80201  
Phone: 303-977-5845  
Fax: 303-971-4306  
email: [ray.j.perez@lmco.com](mailto:ray.j.perez@lmco.com)

### MANAGING EDITOR

Richard W. Adler  
Naval Postgraduate School/ECE Dept.  
Code ECAB, 833 Dyer Road,  
Monterey, CA 93943-5121  
Fax: 831-649-0300  
Phone: 831-646-1111  
email: [rwa@att.biz](mailto:rwa@att.biz)

## EDITORS

### CEM NEWS FROM EUROPE

Tony Brown  
University of Manchester  
PO Box 88 Sackville Street  
Manchester M60 1QD United Kingdom  
Phone: +44 (0) 161-200-4779  
Fax: +44 (0) 161-200-8712  
email: [Anthony.brown@manchester.ac.uk](mailto:Anthony.brown@manchester.ac.uk)

### TECHNICAL FEATURE ARTICLE

Andy Drozd  
ANDRO Consulting Services  
PO Box 543  
Rome, NY 13442-0543  
Phone: 315-337-4396  
Fax: 314-337-4396  
email: [androl@aol.com](mailto:androl@aol.com)

### THE PRACTICAL CEMIST

W. Perry Wheless, Jr.  
University of Alabama  
PO Box 11134  
Tuscaloosa, AL 35486-3008  
Phone: 205-348-1757  
Fax: 205-348-6959  
email: [wwheless@coe.eng.ua.edu](mailto:wwheless@coe.eng.ua.edu)

### MODELER'S NOTES

Gerald Burke  
Lawrence Livermore National Labs.  
Box 5504/L-156  
Livermore, CA 94550  
Phone: 510-422-8414  
Fax: 510-422-3013  
email: [burke2@llnl.gov](mailto:burke2@llnl.gov)

### PERSPECTIVES IN CEM

Alistair Duffy  
School of Engineering and Technology  
De Montfort University  
The Gateway  
Leicester, UK LE1 9BH  
+44(0)116 257 7056  
[apd@dmu.ac.uk](mailto:apd@dmu.ac.uk)

### TUTORIAL

Giulio Antonini  
UAq EMC Laboratory  
Department of Electrical Engineering  
University of L'Aquila  
Poggio di Roio, 67040 Italy  
Phone: +39-0862-43446  
email: [antonini@ing.univaq.it](mailto:antonini@ing.univaq.it)

## ACES JOURNAL

### EDITOR IN CHIEF

Atef Elsherbeni  
**Associate Editor-in-Chief Journal**, Alexander Yakovlev  
EE Department, Anderson Hall  
University of Mississippi  
University, MS 38677  
Phone: 662-915-5382  
email: [atef@olemiss.edu](mailto:atef@olemiss.edu)

## NEWSLETTER ARTICLES AND VOLUNTEERS WELCOME

The ACES Newsletter is always looking for articles, letters and short communications of interest to ACES members. All individuals are encouraged to write, suggest or solicit articles either on a one-time or continuing basis. Please contact a Newsletter Editor.

## AUTHORSHIP AND BERNE COPYRIGHT CONVENTION

The opinions, statements and facts contained in this Newsletter are solely the opinions of the authors and/or sources identified with each article. Articles with no author can be attributed to the editors or to the committee head in the case of committee reports. The United States recently became part of the Berne Copyright Convention. Under the Berne Convention, the copyright for an article in this newsletter is legally held by the author(s) of the article since no explicit copyright notice appears in the newsletter.

### BOARD OF DIRECTORS

#### EXECUTIVE COMMITTEE

Osama Mohammed, President  
Tapan Sakar, Vice President  
Leo Kemple, Secretary

Allen W. Glisson, Treasurer  
Richard W. Adler, Executive Officer

#### DIRECTORS-AT-LARGE

Leo Kemple	2006	Randy Haupt	2007	Atef Elsherbeni	2008
Osama Mohammed	2006	Juan Mosig	2007	Michiko Kuroda	2008
Tapan Sarkar	2006	Omar Ramahi	2007	Eric Mokole	2008

### ACES ELECTRONIC PUBLISHING GROUP

Atef Elsherbeni	Electronic Publishing Managing Editor
Matthew J. Inman	Site Administrator
Orin H. Council	Contributing Staff
Imran Kader	Past Site Administrator
Brad Baker	Past Staff
Jessica Drewrey	Past Staff
Chris Riley	Past Staff

Visit us on line at:  
<http://aces.ee.olemiss.edu>

## **Election Committee Report**

Rene Allard

The 2005 Board of Directors election was closed on August 31,2005. The following individuals were elected to a three year term.

Leo Kempel  
Osama Mohammed  
Natalia Nikolova

## A New Modelling Army?

Alistair Duffy, De Montfort University, Leicester UK [apd@dmu.ac.uk](mailto:apd@dmu.ac.uk)

About 460 years ago, during the English Civil War, the New Model Army was formed. It was well organised, the soldiers were well disciplined, regularly paid and well trained. The 22000 soldiers became known as the Ironsides and the New Model Army was a huge influence on government for quite a number of years.

So, although there is a small play on words in the title, this contribution to *Perspectives in CEM* aims to ask how we can better coordinate our army of modellers, how we can ensure they are correctly trained and disciplined. The latter is not referring to self-control but the organisation of the CEM discipline.

What I want to do is to put forward a view about electromagnetics education in this issue and, in the next issue of the Newsletter, compile views that have come to me as a result of this essay, whether supporting, criticising or simply offering another perspective.

As in any form of organisation, different roles need to be played out by different people. So does this imply that when it comes to modelling, everyone should expect to get the same education? In the UK we talk of Chartered Engineers, Incorporated Engineers and Engineering Technicians, while the formal explanations and definitions are more precise and involved ([http://www.engc.org.uk/Registration/Register\\_Sections.aspx](http://www.engc.org.uk/Registration/Register_Sections.aspx)) a useful summary is that Chartered Engineers *introduce new technology*, Incorporated Engineers *apply new technology*, and Engineering Technicians *have the skills to get the job done*. While this is a very UK-centric view, I hope the distinctions translate across borders reasonably well.

If we take the view that modelling could be similarly organised, a broad structure could be that modellers will fall into one of the two broad groups:

- Creators. These will develop new techniques, enhance techniques, create packages, develop strategies for modelling structures or provide detailed (mathematical) interpretation of results.
- Implementers. These will use implement models, process the results, undertake sensitivity analyses, etc.

The skills and knowledge of these groups are different; the expectations of them are different but perhaps there is a tacit expectation when it comes to educating them that they are slightly different roles for the same people and therefore the same level and content of education is required.

The traditional approach to teaching electromagnetics is to give a thorough, mathematically based grounding in electro- and magnetostatics, moving on to Maxwell's equations and then using these simple ("a moment to learn, a lifetime to master") equations to study propagation in plane and guided media, antennas and other structures. Once past the almost Herculean task of mathematically analyzing a half wave dipole, students are then permitted to use a modelling package in anger. Of course, in their assignments, they must explain how the governing

mathematics of the particular technique give rise to the results displayed. Naturally, simulation and animation tools (such as some of those available through ACES) can be valuable in helping visualisation but the emphasis is, and must be, on a thorough mathematical basis.

In the last 30 years, society itself has changed considerably. We now live in a world of pervasive and passive entertainment. Although there are statistics that ‘prove’ the assertion both ways, a common complaint in the University sector is that there is a constant decline in the mathematical abilities of students entering Higher Education. Also, within this timeframe, the importance of electromagnetics to electrical and electronic engineers in general has increased, for example, electromagnetic compatibility is an issue for most electronic engineers, whether they realise it or not. There is, therefore, a greater pervasiveness of electromagnetics knowledge required in industry. Hence, pretty much all students need to have a good working understanding of electromagnetics, and this should not be limited to the relative few with the ability to visualise the abstractness. Not all of these students will have the love of mathematics that is demanded of a traditional study of electromagnetics. It is also an interesting observation that many with relevant mathematical skills are actually opting to read one of the more fashionable courses such as Media Technology (certainly in the UK). Another factor that needs to be considered is that computers are much more of a tool than they were: clever GUIs and the multi-billion dollar games industry mean students can readily enter a virtual world without a second thought.

So taking some of these factors together we see that more students need to understand electromagnetics but the overall lower mathematical ability (even without accepting the assertion of declining ability, a bigger group suggests a lower group average) means that the traditional approach of starting with the mathematics and then moving to modelling, to make life easier, is now inappropriate. The wider use of electromagnetics as a general design tool suggests that there are two main groups of EM engineers: the Creators and the Implementers, with the different expectations of their knowledge and skills. Does this suggest that we need to turn a standard electromagnetics curriculum on its head?

Perhaps a better approach would be to work ‘backwards’ and start with modelling and using this to build a knowledge of field behaviour. Working from a modelling base, this would allow students to develop the tacit knowledge that dictates the ability to understand how to model, what the results mean in a practical sense and how reliable they are. After all, a carpenter will learn, through trial and error, practice and through the guidance of an expert, how to work wood. He is unlikely to spend many hours studying the theory of complex natural polymers.

In such an approach, perhaps a starting point would be to look at field coupling between two closely spaced antennas, or fields within a motor. Visualising the fields would be a good way to introduce field properties and behaviour, leading on to many other essential aspects. After a structured programme of work developing a good understanding of the model behaviour, looking at the factors that influence the results and visualising the performance, students should be quite competent Implementers. At this stage, the mathematical analysis can be undertaken in earnest. Those without the requisite mathematical knowledge will still have a useful skills set and those with the mathematical skills will be better able to develop a more comprehensive understanding of the meaning of the equations.

So, in creating our New Modelling Army, we should concentrate on the models first and the mathematics last. A possible argument against this is that “surely, if students can’t do the mathematics, they will not be able to understand the results”. The same sort of criticism was laid at the door of Kepler when he created a table of logarithms based on Napier’s work, he was essentially told that unless you can do the calculations all yourself, you can’t trust them. When was the last time you created your own table of logarithms, or even checked that the number coming out of your calculator or computer package was correct?

Should we concentrate on developing practical skills, first, in the many and mathematical skills later in the few? Perhaps it is time to move on, and concentrate on ensuring that more students have skills in doing the basics, such as simulating and visualising field behaviour and are able to identify when something is ‘not quite right’ or understand the basic limitations of their chosen modelling approach. Of those that get beyond a general understanding of fields, they can be more formally educated with a strong mathematical and analytical understanding. In doing this our New Modelling Army will be well trained, well organised and the discipline itself will be well constructed. Hopefully, our Ironsides will be well and regularly paid and will be able cast their influence widely and for a long time.

If you (dis)agree with anything here, have an alternative view or any experience of teaching electromagnetics to support or contradict this essay, please contact us so your views can be included in the next issue of the newsletter (contact [apd@dmu.ac.uk](mailto:apd@dmu.ac.uk) or [barch@us.ibm.com](mailto:barch@us.ibm.com)). Unless you say otherwise, we will assume that you are happy to have your comments attributed.

# HF Fractal Wire Antenna Case Study

W. Perry Wheless, Jr. and Michael A. McNees  
 Department of Electrical and Computer Engineering  
 The University of Alabama  
 Tuscaloosa, AL 35487  
 Email: wwheless@eng.ua.edu

**Abstract**—A HF fractal wire antenna case study is reported here. SWR and radiation pattern results for two realizations of a particular fractal geometry, plus a plain bowtie implementation for comparison, are presented. Sufficient quantitative results are shown to effectively aid a radio communicator contemplating the potential merits of deploying a fractal wire dipole to significantly lower the fundamental resonant frequency for a specified antenna length from that of a classical single-wire  $\frac{\lambda}{2}$  dipole.

## I. INTRODUCTION

There is always considerable interest in the amateur radio community in compact wire antenna candidates for the 1.8 - 2.0 MHz (160 m) and 3.5 - 4.0 MHz (80 m) bands because the long lengths associated with classical dipole antennas for these bands are prohibitive for many prospective users. Also, there are considerable numbers of other practical communicators who use the HF spectrum for their radio communication systems. First thought may go to antenna length, but close behind in priority come considerations of gain, radiation pattern, and overall competitiveness with full-sized classical dipoles.

An overview or tutorial on fractal antennas is outside the scope of this work. There are many references available to the interested reader, including references [1]-[8] cited at the end of this paper. Additional information is also available from a number of Web sites, including [www.fractenna.com](http://www.fractenna.com).

The fractal shape selected for this engineering study is illustrated in Figure 3 of [1]. The corresponding basic "building block" version, constructed entirely with wires, is shown in Figure 1. In Figure 1, the individual wires are numbered, the antenna is in the  $y$ - $z$  plane, the center of the wire is at  $z = 22$  feet, the antenna length is 33 feet (32 feet plus a 1-foot wide feed-point wire at the center, wire #31), and the respective maximum and minimum heights of the antenna ends are 30 feet and 14 feet.

To obtain SWR and radiation patterns for all antenna variations in this paper, Roy Lewallen's EZNEC version 4.0 [9] provided the numerical analysis. For all EZNEC results reported here, real/high accuracy ground was selected with  $\sigma = 3$  mS/m and  $\epsilon_r = 12$ , typical of west central Alabama soil conditions. Also, "copper" wire loss was selected, so the results here include conductor loss. In all cases, these planar antennas are placed in the  $y - z$  plane at  $x = 0$ , with + $y$  corresponding to the compass direction North, and + $x$  corresponding to the compass direction East. Therefore, in visualizing the radiation from these example antennas in the

real world, azimuth angle  $\varphi = 0^\circ$  is toward the East,  $\varphi = 90^\circ$  is toward the North, and so forth.

## II. BASIC FRACTAL DIPOLE CHARACTERIZATION

For the basic fractal dipole shown in Figure 1 and described above, the SWR plot obtained by use of the EZNEC code for 1.75 to 30 MHz in steps of 0.25 MHz is given in Figure 2. Note that a feeding transmission line characteristic impedance of  $Z_0 = 50 \Omega$  was used as reference for the SWR calculations.

It would be expected that qualitative features of the plot will change if an alternative  $Z_0$  is used and, for illustration, Figure 3 shows the corresponding plot with the alternate  $Z_0 = 25 \Omega$  applied.

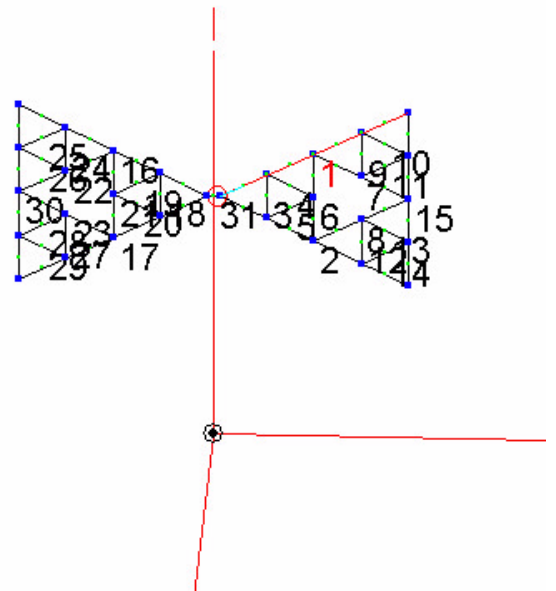


Fig. 1. Basic fractal dipole geometry.

The fundamental resonant frequency for the basic fractal dipole is close to 8.25 MHz. This may be compared to the resonant frequency of a single-wire dipole of the same length (33 feet) obtained from

$$f_{0d} = \frac{468}{\ell}$$

where  $f_0$  is half-wave resonant frequency in MHz,  $\ell$  is the antenna length in feet, and the formula takes into account end effect. By this formula,  $f_0$  comes out to be 14.2 MHz, and so the fractal dipole geometry reduces the fundamental resonant frequency by approximately 42%.

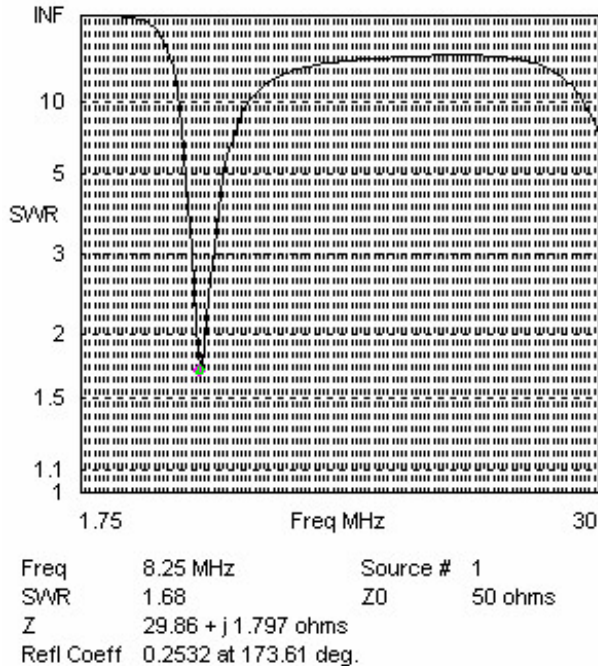


Fig. 2. Basic fractal dipole SWR,  $Z_0 = 50$ .

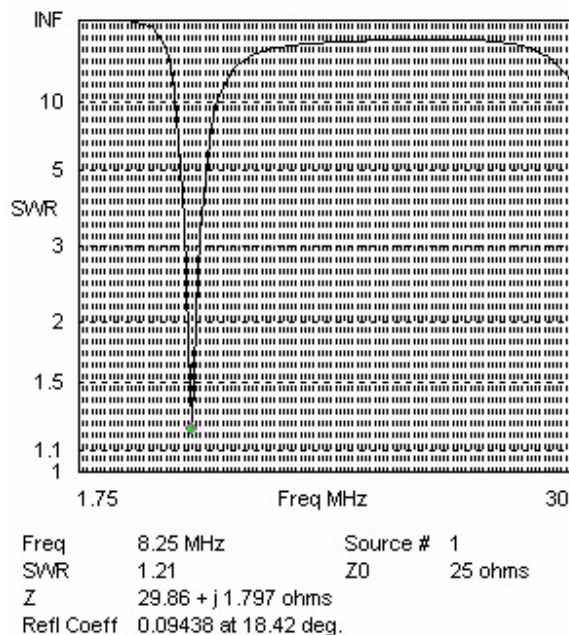


Fig. 3. Basic fractal dipole SWR,  $Z_0 = 25$ .

The major prices paid for this reduction in resonant frequency are that the dipole ends are now 16 feet tall, and some 31 wires are now involved in the place of one. As for radiation efficiency, an elevation plot in the East-West plane (recall the antenna is oriented on a North-South line) is shown in Figure 4 and the corresponding North-South pattern is in Figure 5.

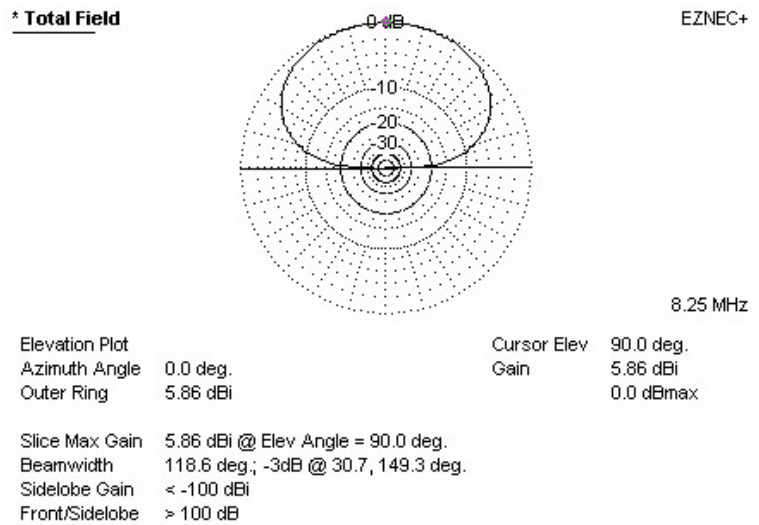


Fig. 4. East-West elevation plot, 8.25 MHz.

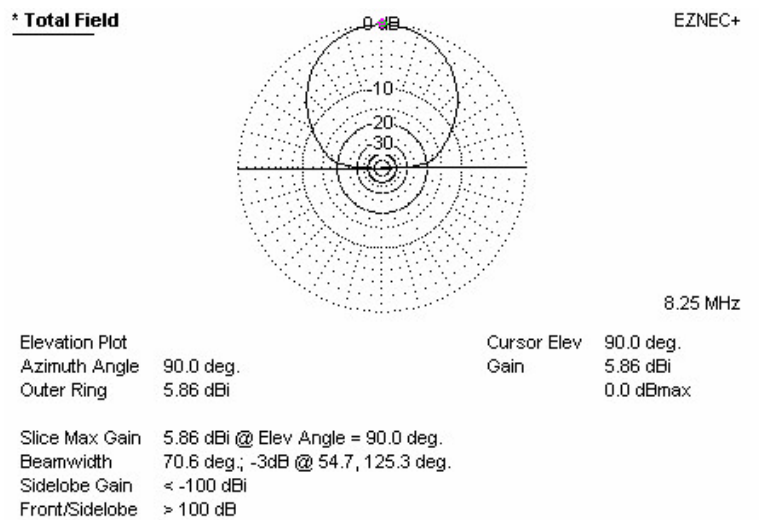


Fig. 5. North-South elevation plot, 8.25 MHz.

### III. COMPOUND FRACTAL DIPOLE

The second illustrative analysis to be presented is that of a "compound fractal dipole," comprising a total of six of the building block geometries used to make the basic fractal dipole

antenna considered above. The EZNEC view of the antenna geometry is seen in Figure 6.

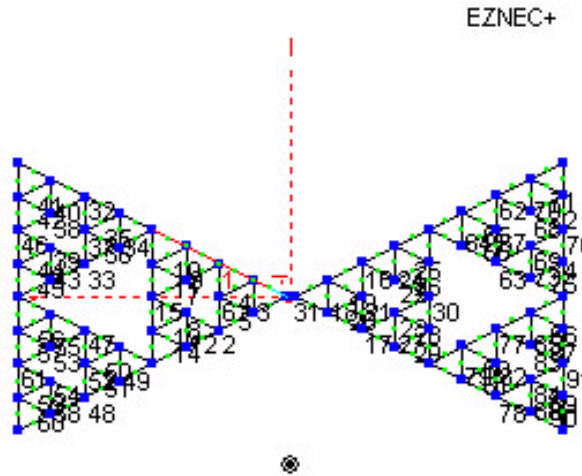


Fig. 6. Compound fractal dipole geometry.

Here, the length of the dipole is 65 feet, and the height of the ends is 32 feet. The composite structure is comprised of some 91 wires. Again, the antenna is placed on a North-South line, and the center is at height  $z = 22$  feet, so the maximum height of the ends is 38 feet and the minimum height of the ends is 6 feet above ground. The HF SWR plot, again in 0.25 MHz steps and for  $Z_0 = 50 \Omega$ , may be seen in Figure 7. In this case, an interesting alternative plot results from choosing  $Z_0 = 600 \Omega$  (Figure 8), of practical interest because many HF dipoles are fed with  $600 \Omega$  ladder line. Note in Figure 8 that the fundamental resonant frequency has become obscured, but that the SWR exhibits a favorable characteristic curve over most higher frequencies in the HF spectrum.

The fundamental resonant frequency is about 4 MHz, in contrast to a classical wire dipole resonant frequency of about

$$f_{0d} = \frac{468}{65} = 7.2 \text{ MHz.}$$

Therefore, in this case, the resonant frequency has been lowered by approximately 44.4%. Clearly the resonant frequency has been cut nearly in half compared to the single-wire dipole, but dealing with ends that are now 32 feet tall becomes a mechanical issue of increasing concern and implementation difficulty. On the other hand, since  $600 \Omega$  ladder line feed at HF has insignificant loss properties and 10:1 SWR is not considered problematic with ladder line feed, it is apparent that this variation of the fractal dipole antenna exhibits favorable SWR characteristics over most of the HF spectrum. Unfortunately, in the  $Z_0 = 600$  case the low frequency SWR becomes elevated to values considerably above 10:1 so that

only the amateur bands 40m - 10m benefit significantly from the broadband low SWR behavior.

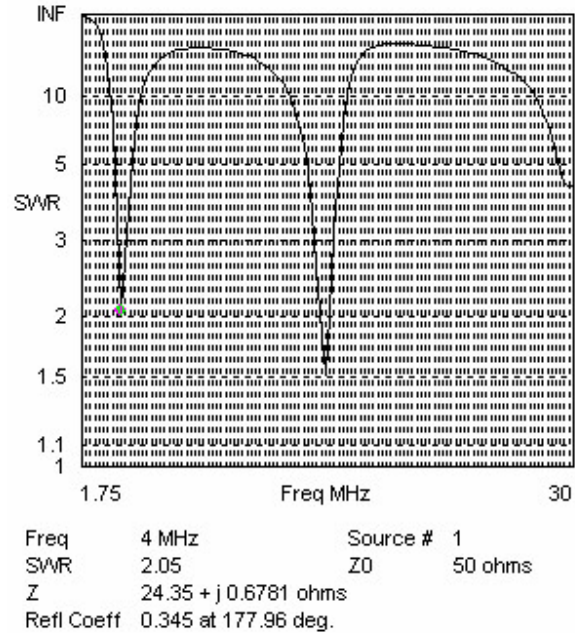


Fig. 7. Compound fractal dipole SWR,  $Z_0 = 50$ .

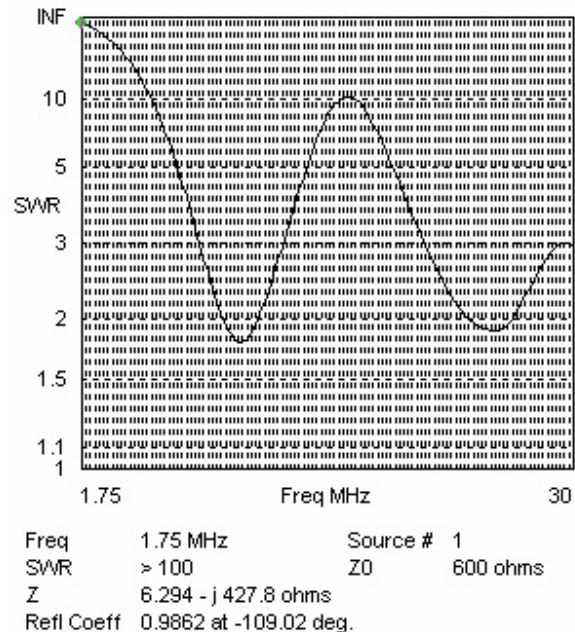


Fig. 8. Compound dipole SWR,  $Z_0 = 600$ .

An East-West elevation plot (broadside to the antenna deployment) and North-South elevation pattern plot (in the plane of the antenna) follow, as Figures 9 and 10, respectively.

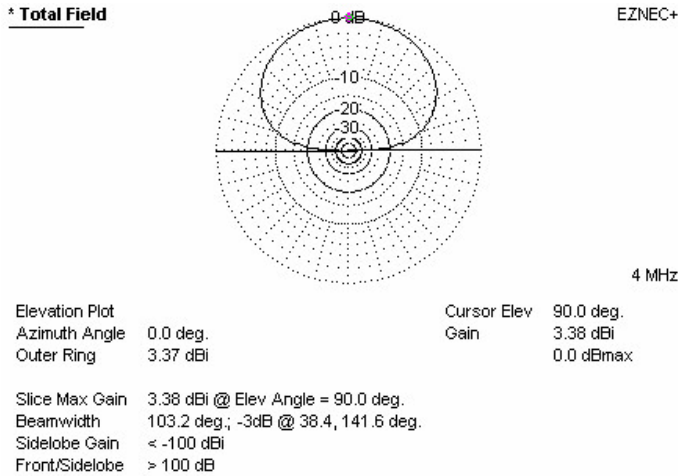


Fig. 9. East-West elevation plot, 4 MHz.

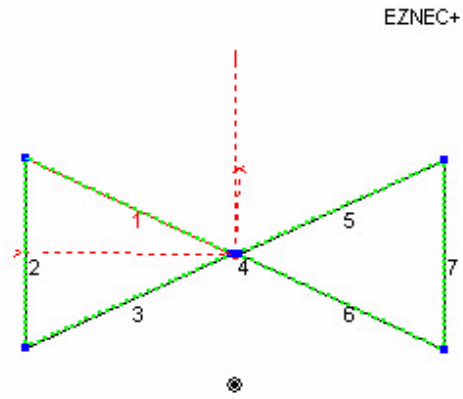


Fig. 11. Plain HF bowtie antenna.

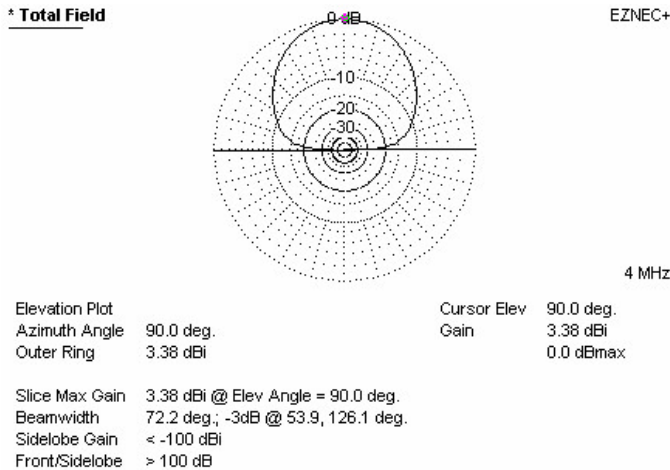


Fig. 10. North-South elevation plot, 4 MHz.

The gain of 3.4 dBi and the radiation patterns, computed above real ground as noted earlier, compare quite favorably with those of a classical dipole at the same height as the compound fractal dipole's (center) feed height.

#### IV. PLAIN HF BOWTIE

A natural question is to ask how much the "frill" associated with the fractal geometry contributes to lowering the resonant frequency for a dipole of given length. Some initial insight into the matter is gained by an analysis of the bowtie skeleton associated with the compound fractal dipole analyzed and discussed above. The internal (fractal geometry) wires were removed, leaving a frame of seven wires (again including a one-foot connector wire at the center for applying the rf feed) as shown in Figure 11 below.

To facilitate a fair comparison, this antenna is the same length as the compound fractal dipole (65 feet), has its center at the same height above ground (at  $z = 22$  feet) and has ends that are the same height (maximum elevation at  $z = 38$  and minimum elevation at  $z = 6$  feet). The EZNEC analysis was made using real ground parameters of  $\sigma = 3$  mS/m and  $\epsilon_r = 12$ , the consistent practice throughout this study. The resulting HF SWR plots for  $Z_0 = 50$  and  $Z_0 = 600 \Omega$  may be seen in Figures 12 and 13. As indicated in Figure 12, the fundamental resonant frequency is now about 4.5 MHz, approximately 37.5% lower than that of a classical single-wire dipole of the same length.

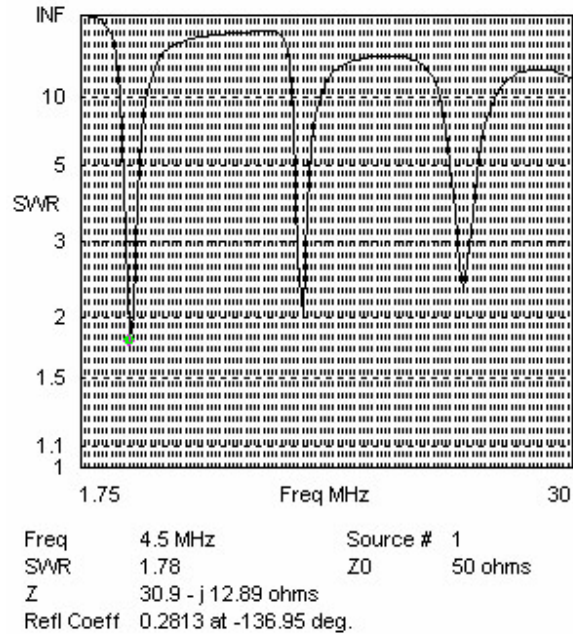


Fig. 12. HF bowtie SWR,  $Z_0 = 50$ .

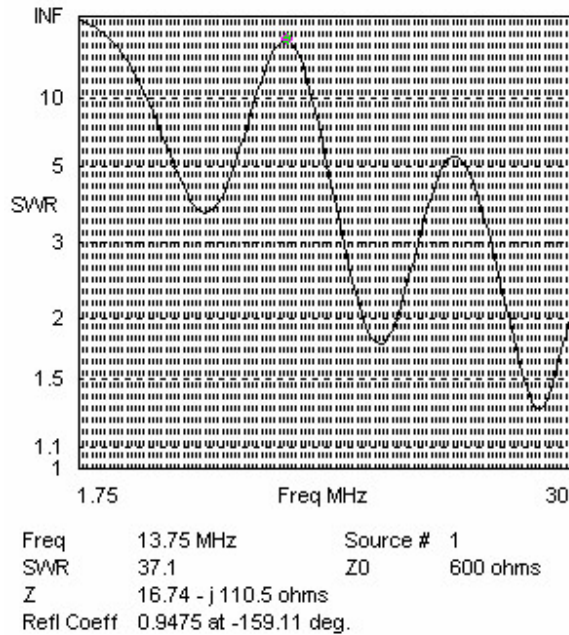


Fig. 13. HF bowtie SWR, Z0 = 600.

Elevation plots at  $\varphi = 0^\circ$  (East-West) and  $\varphi = 90^\circ$  (North-South) are presented in Figures 14 and 15.

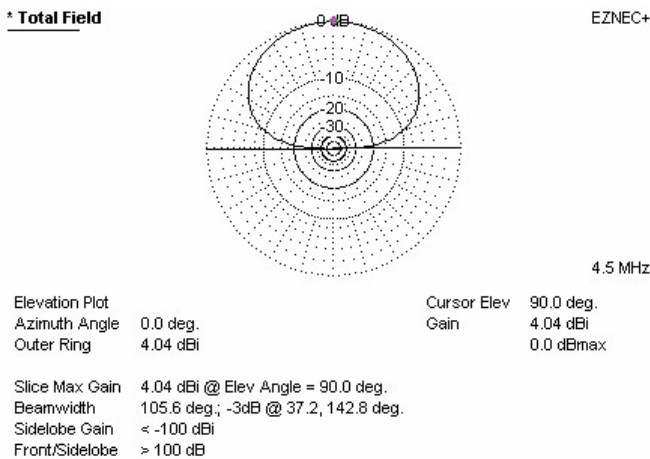


Fig. 14. East-West elevation plot, 4.5 MHz.

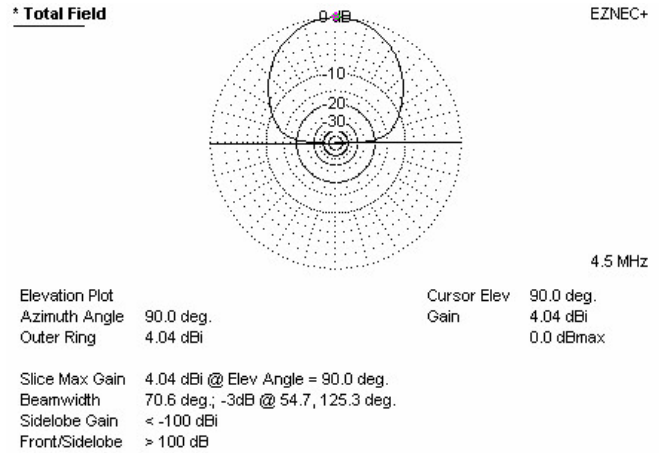


Fig. 15. North-South elevation plot, 4.5 MHz.

Notable differences from those for the compound fractal dipole are that the fundamental resonance has shifted up by about 0.5 MHz, from the vicinity of 4.0 to about 4.5 MHz, and the maximum gain for the plain bowtie at its resonant frequency is greater by more than 0.5 dB.

## V. CONCLUDING REMARKS

From this engineering study of limited scope, it appears that reduction in resonant frequency follows mostly from flaring out the two dipole sides, and here the plain HF bowtie was rather effective in achieving a lower resonance for a given dipole length. Essentially, if the length decreases, the governing fundamental physics seems to require an associated breakout in the other dimension (width) of appropriate extent in order to maintain rough parity with the classical full length single-wire dipole. The further reduction in resonance achieved by adding the detailed frill of a fractal geometry interior to the bowtie skeleton may be second-order, but it is nonetheless significant and potentially worthwhile.

Where the available antenna deployment space is limited, but adequate, a 7-wire bowtie has some attractive SWR and radiation characteristics for 80m and 160m band use. In cases where the available length is insufficient for the plain frame bowtie, adding the fractal wire geometry inside the frame both lowers the antenna's resonant frequency further and provides an interesting conversation piece for its owner.

A 160m (1.9 MHz) extension of the shaping geometry considered here would require an available length of about 154 feet for the bowtie, with ends that are approximately 76 feet high, compared with a length requirement of about 137 feet and ends that are approximately 68 feet in height for the compound fractal variation. There will be instances where the available supports or length preclude the extra 17 feet of length and/or 8 feet of height required by the plain bowtie, but would accommodate the smaller dimensions of the compound fractal dipole geometry.

This report is merely one particular case study, and does not make any general claims with respect to electrical properties, performance, and overall merit of fractal versus classical antenna realizations. Further, the figures reported in this paper are strictly from computer-based numerical modeling and no experimental data is available for these antennas.

The interested reader is encouraged to further explore the emerging world of fractal antennas by studying readily available references treating their background, theory, and desirable properties. Finally, all readers should be made aware that certain commercial interests in the manufacture and sale of fractal antennas are protected by a number of patents that have already been granted (see [1], for example).

#### REFERENCES

- [1] Cohen, Nathan, "Fractals' new era in military antenna design," *Defense Electronics*, August 2005, pp. 12-17.
- [2] Barnsley, M., *Fractals Everywhere*, Academic Press, London: 1988.
- [3] Cohen, N.L., "Fractal antennas Part I," *Communications Quarterly*, Summer 1995, pp. 5-23.
- [4] Hohlfeld, R.G. and Cohen, N.L., "Self similarity and the geometric requirements for frequency independence in antenna," *Fractals*, **7** (1999), pp. 79-84.
- [5] J. Anguera et al., "The Fractal Hilbert Monopole: A Two-Dimensional Wire," *Microwave and Optical Tech. Lett.* **36**, 2102 (2003).
- [6] Best, S.R. and Morrow, J.D., "The effectiveness of space-filling fractal geometry in lowering resonant frequency," *Antennas and Wireless Propagation Letters*, Volume: 1, Issue: 5, 2002, p 112 - 115.
- [7] Vinoy, K.J., Jose, K.A., Varadan, V.K., and Varadan, V.V., "Resonant frequency of Hilbert curve fractal antennas," *Antennas and Propagation Society International Symposium*, 2001. IEEE, Volume: 3, 8-13 July 2001, p 648 - 651.
- [8] Vinoy, K.J., Abraham, J.K., and Varadan, V.K., "Fractal dimension and frequency response of fractal shaped antennas," *Antennas and Propagation Society International Symposium*, 2003. IEEE, Volume: 4, 22-27 June 2003, p 222 - 225.
- [9] EZNEC is a software product of Roy Lewallen, as described at <http://www.eznec.com/>.

# THE COMPUTATIONAL ELECTROMAGNETIC MODELING FRAMEWORK

Edgar L. Coffey, III  
Advanced Electromagnetics  
*bcoffey@gemacs.com*

## Abstract

The Computational Electromagnetic Modeling Framework is an EM simulation and development platform that increases the productivity of all participants in the electromagnetic analysis of a complex system. It provides a collaborative engineering environment in which the participants easily construct simulation inputs, share and re-use data, create computational capabilities that utilize a suite of computational EM modeling tools, and produce engineering results from the electromagnetic simulation inputs. This article describes the basic capabilities of the *Framework* and offers a simple modeling example to demonstrate its usefulness.

## INTRODUCTION

Recent paradigm shifts in the EM modeling and simulation community have indicated that fewer analysts want to use computational EM software unassisted by some kind of graphical user interface. Most GUIs, however, are built around a specific CEM code and can be used only with that particular piece of software.

The CEM Framework eschews this “code centric” approach for one that is more “data centric,” as shown in figure 1. The GUI tools are designed

around the roles of the analysts: building models, generating simulation scenarios, and post processing/visualization. The tools are linked via a set of common data structures, and data generated by the tools can be stored in a central data repository if desired. The CEM codes themselves become additional tools in the Framework suite. This code-agnostic, data-centric approach means that an EM analyst can use the Framework across a number of CEM software tools.

## CAPABILITIES

As alluded to in figure 1, the individual Framework tools are application-specific to the needs of the participants in a CEM analysis. In that sense the Framework shields the user from having to know the details of the underlying CEM software tools that perhaps only a developer would know. This lets the Framework user perform his/her functions in a CEM code-independent way, committing to a particular CEM code only just before running that code.

The CEM Framework was originally built with the GEMACS software suite in mind, and the full power of the Framework can be brought to bear on GEMACS-specific problems. However, the tools themselves can be and have been utilized with other CEM codes, as the discussion that follows will illustrate.

## Building Electromagnetic Models

The construction of valid electromagnetic models is one of the most time consuming tasks facing an EM analyst. Models generated by CAD programs may be suitable for visualization, mechanical analysis, or other applications, but they generally do not obey the rules of electromagnetic modeling. Consequently, they must be significantly modified before being submitted to a CEM software tool.

The CEM Framework’s *AutoGridder* application translates constructive solid geometry (CSG) CAD

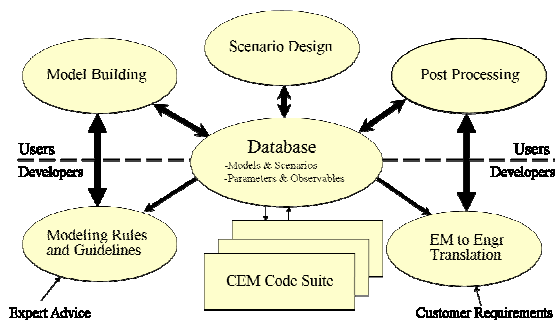


Figure 1. Overview of the CEM Framework.

models into CEM-valid electromagnetic models, as shown in figure 2. The CSG geometry represents an “abstract description” of the model’s surface to *AutoGridder*, which then creates a mostly uniform mesh of mostly quadrilateral elements over the surface of the model. The result is a whole-object, fully-connected mesh suitable for submission to a number of CEM codes, including GEMACS, NEC, and others.

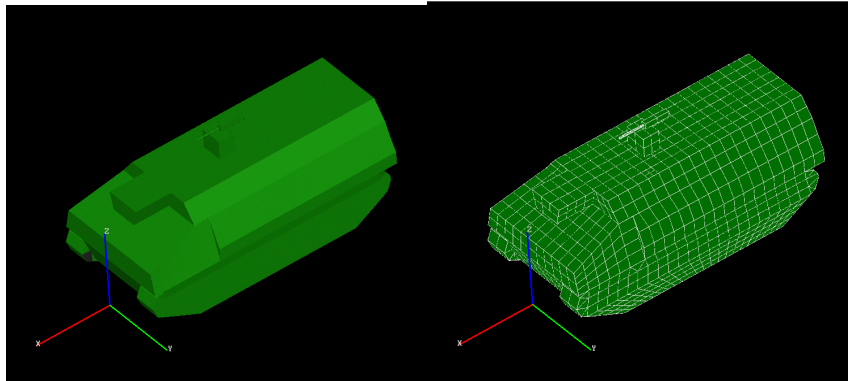


Figure 2. *AutoGridder* Conversion of a Solid CSG Model into a CEM-valid Electromagnetic Model.

### Creating Simulation Scenarios

Since electromagnetic phenomena are “invisible,” it is difficult sometimes to imagine the modeling scenario one is trying to create. The Framework’s *Application Builder* tool lets the EM analyst create modeling scenes visually by adding the various modeling elements to a 3D viewer and moving or manipulating those elements, assigning electromagnetic properties to those elements, and finally executing a CEM code by exporting the visual scene into inputs the code will accept. Figure 3 shows a ground vehicle in a scene to which a ground plane has been added. The hemispherical grid represents the analyst’s request for far-field pattern data. Removed from figure 3 for clarity but present in the actual simulation are the radiating antenna, its excitation, and other elements in the scene. When the analyst is satisfied with the scene, he/she exports it to a CEM code to obtain the re-

quested observables, in this case the far-field pattern data.

### Obtaining Meaningful Results

The majority of CEM codes are pure “number crunchers.” They can generate vast amounts of data but have no way of rendering that data in a format easily grasped by the analyst. More importantly perhaps is the typical case when the analyst doesn’t want the raw CEM output of the code but needs a higher-level observable instead, such as antenna gain, EMC margin, or probability of mission success.

The Framework’s *Component View* data post processor is able to extract data from CEM results and format that data in a variety of ways as directed by the user, not by a set of canned, static dialog boxes and menu options.

This application is named *Component View* because of its use of modeling components (called modules or “glyphs”) in a workflow paradigm as shown in figure 4. Each glyph performs a specific

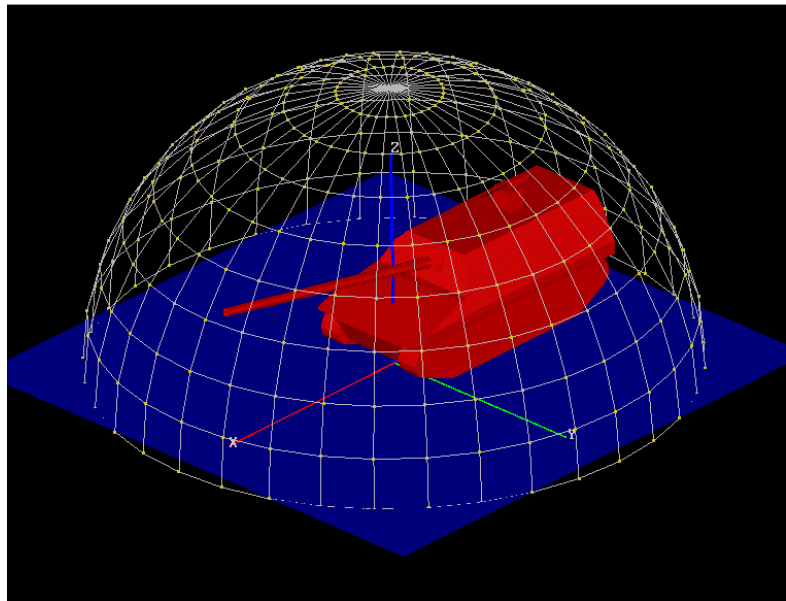


Figure 3. *Application Builder* Screenshot Showing a Scenario to be Submitted to a CEM Code.

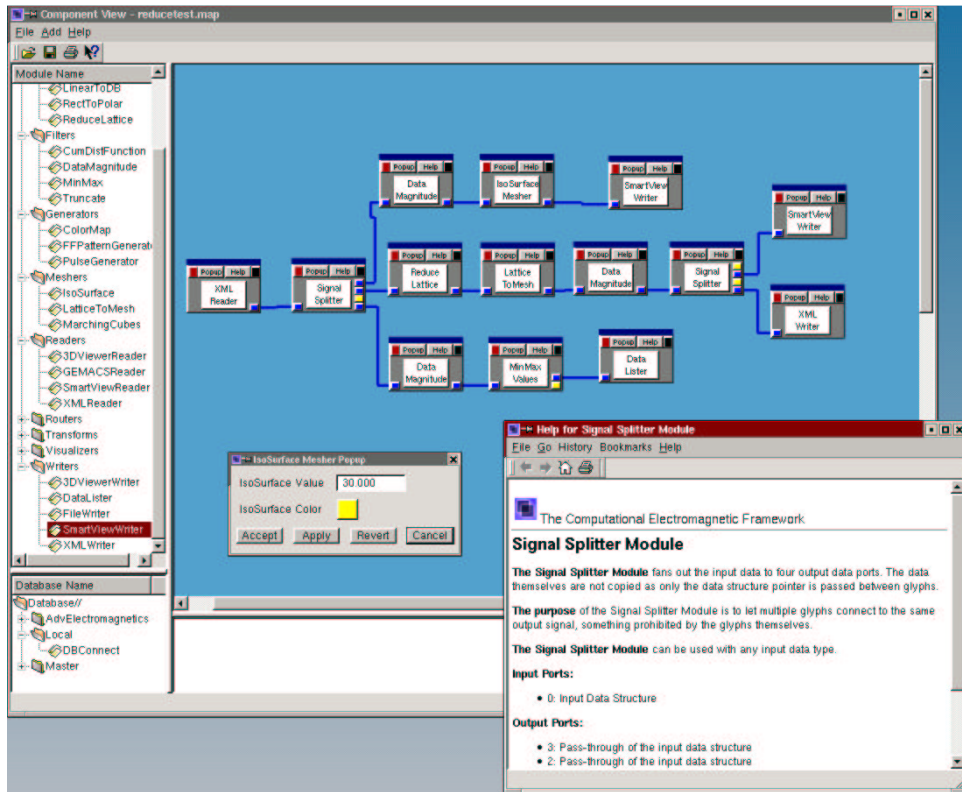


Figure 4. *Component View* Screenshot Showing Component Lists, Workflow Paradigm, Help Viewer, and a Typical Programmable Popup Box.

function, and the glyphs are connected together as shown to generate the results required by the analyst.

The workflow in figure 4 is being used to generate three different renderings of 3D volumetric fields inside a cavity geometry. Each rendering is represented by a different path in the figure.

The functionality of *Component View* can be extended by the user, as the user can write his/her own glyphs, compile them into dynamic load libraries, and drop them in the *Component View* glyph folder. A separate Glyph Development Kit is available to interface the user's software to the *Component View* C++ objects and data structures.

## Visualization of Results

Augmenting the Framework applications described above is a three-dimensional visualizer called *SmartView*, an XY plotting routine, and a polar plotting routine. *SmartView* is a general three-dimensional renderer and graphical editor with transparency capabilities. While very useful in an

electromagnetic analysis, it is not limited to that and can be used in other engineering and scientific disciplines as well.

Figure 5 shows how the *SmartView* too has rendered the results of a *Component View* simulation. The vehicle from figure 2 is radiating 50 watts of power from a whip antenna (difficult to see in the figure). The yellow and red surfaces represent iso-contours of field strength at 2 V/m and 5 V/m respectively. The raw data were generated from an *Application Builder* scene in which electric fields were requested

within an 80m x 80m x 25 m lattice with spacing every 2 meters. The raw data were generated by the GEMACS software, output in XML format, and input to *Component View*, which performed the iso-surface computation at each field strength level, converted the results to meshes for visuali-

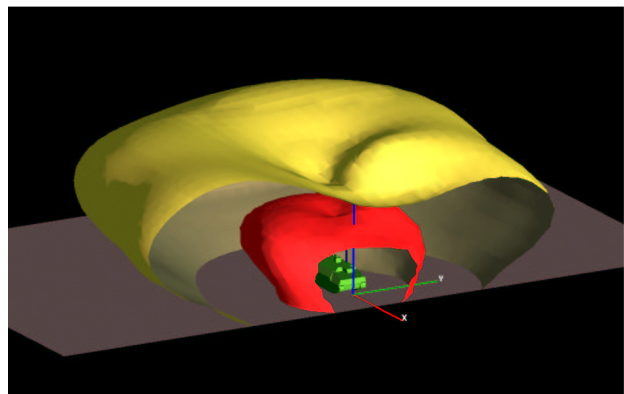


Figure 5. Screenshot of a *SmartView* Rendering of Iso-Surface Contours Around a Ground Vehicle with Radiating Antenna.

zation, and combined the two contours with the original geometry for rendering with *SmartView*.

## Validating Geometry Models

*SmartView*'s "error" mode evaluates the integrity of a meshed model against a number of rules set by the user, and *SmartView*'s "edit" mode lets the user fix any problems by using simple editing functions.

The *SmartView* user is able to set about 40 geometry integrity criteria via a set of dialog boxes such as the one shown in figure 6. These integrity settings including the size and shape of surface patches, wire segment lengths, adjacent patch ratios, wire/radius ratios, junction ratios, and other common electromagnetic modeling values. For many criteria, the user is able to set "good", "warning", and "error" ranges, as indicated by the green/yellow/red bars in figure 6.

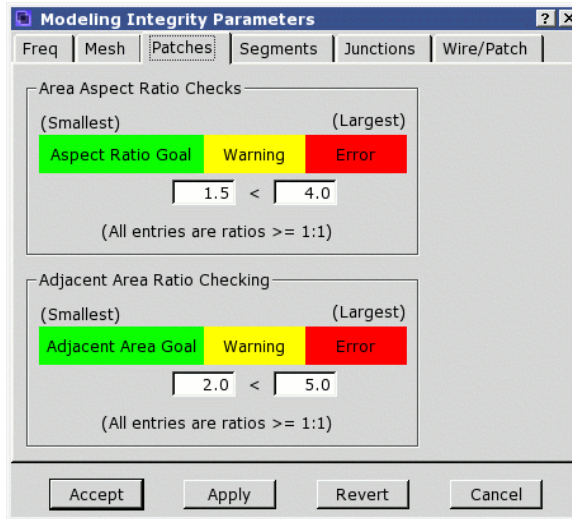


Figure 6. One of Six Dialogs in Which a User Sets *SmartView* Integrity Criteria.

When *SmartView* evaluates a geometry model for errors, it color-codes the surface patches and wire segments with the same green/yellow/red coding. The result is a geometry rendering that is color coded for quick identification of problem areas. Figure 7 shows such a rendering of a simplified aircraft model. When a user double clicks on a

patch or wire segment, a dialog box appears, listing the warnings and errors that *SmartView* has found for that particular modeling element.

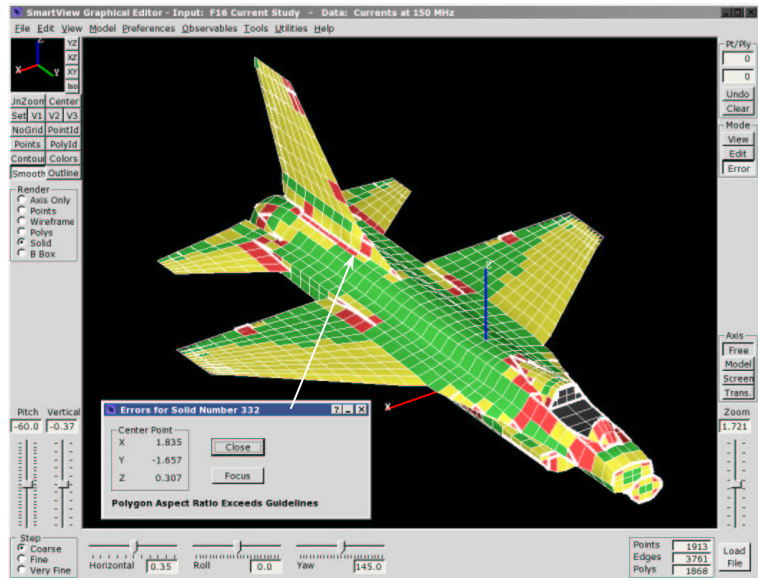


Figure 7. Error Display in *SmartView* Showing Green, Yellow, and Red Coloring and an Error Popup Window.

*SmartView*'s editing features are difficult to describe in a static venue such as this article, so the more powerful features will just be listed.

- Add, remove, and edit patches and wires
- Combine two patches at common edge
- Split a patch into two patches
- Split an edge into two or three edges
- Move a point along the surface
- Find "flipped" surface normals
- Find "disconnected" patches and wires

In addition to these graphical editing features, *SmartView* has a large number of non-graphical editing capabilities. The user can copy a model or a portion of a model and paste it into another model. There are translation, rotation, and scaling tools that operate on all or part of a model. A model's mesh can be reduced via decimation tools or re-meshed/refined by using a tessellation tool.

*SmartView* accepts inputs and produces outputs in three CAD formats (BYU, STL, and X3D), two CEM code formats (GEMACS, NEC), an XML format, and two native formats. There is also a separate ACAD-to-*SmartView* converter available.

## Getting On-line Help

In addition to the extensive help afforded by each application, the CEM Framework also has a specific *Help Assistant* application. It consists of a set of indexed, hyperlinked pages that contain all Framework documentation, including the complete user manual in PDF format.

## EXAMPLE – ANTENNA PLACEMENT

For this example, we need to determine which of two candidate locations is “best” for siting an antenna on a structure. The structure geometry and antenna sites are shown in figure 8, with the candidate antenna sites denoted by the XYZ axes. One site is on top of the elevated box, while the other site is on the level below the box.

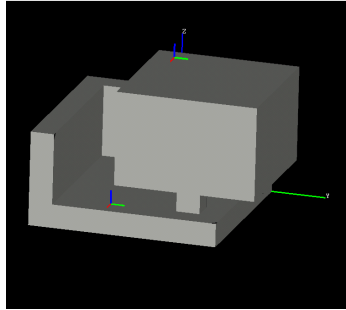


Figure 8. Example Problem

The acceptance criterion is that the directivity of the in-situ pattern should be 0 dBi or greater over the angular extent

$$60^{\circ} \leq \theta \leq 90^{\circ}$$

$$0^{\circ} \leq \phi \leq 360^{\circ}$$

The antenna to be sited is a simple  $\lambda/4$  monopole operating at 200 MHz. It will be driven by a 25 watt source with 50 ohm load. We’ll ask for the following observables, including some for a “sanity check” on our simulation.

- Surface currents induced on the structure
- Far-field pattern
- Comparison of patterns over range of interest

To generate the observables listed above, we’ll go through the following steps using the various CEM Framework tools:

- Generate models of structure and antenna
- Place antennas on structure, excite/load them
- Request EM observables
- Run the CEM code (GEMACS)
- Post process the raw data into observables
- Visualize the data to aid in decision making

## Generating CEM Models – AutoGridder

The structure in figure 8 is easily represented as a CSG model as shown in figure 9. The CSG model is input into the *AutoGridder* tool with a requested mesh size of 0.15m (corresponding to  $\lambda/10$ ). The meshing process takes only a few seconds, producing the GEMACS-compatible mesh shown in figure 10.

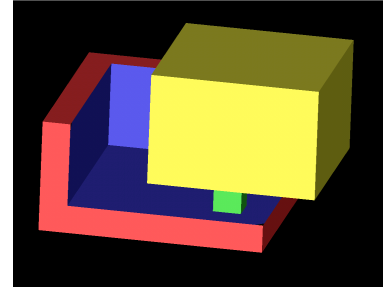


Figure 9. CSG Representation of the Example Problem.

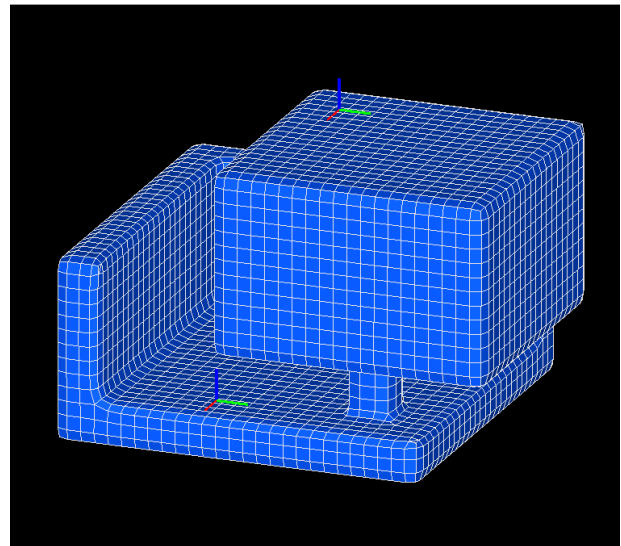


Figure 10. *AutoGridder* Mesh of Figure 9 with Antenna Sites Shown for Reference.

The two monopole antennas are identical, and they are modeled as six-segment wires. The geometry description for them is created by hand.

## The Modeling Scenario – App Builder

Now that we have generated the geometry modeling components (structure, antennas), we have to put them in a “scene” to submit to the CEM code. The scene includes all geometry elements, a ground plane if present, excitations, loads, and observable requests.

*Application Builder* starts with a blank screen into which we will add our modeling elements via dialog box descriptions. We select the elements to be added via a drop down menu list, shown in figure 11. For this scenario, we will use the following elements:

- Box structure (from *AutoGridder*)
- Both antennas (hand generated)
- Excitation of driven antenna
- Loads for both antennas
- Request for surface currents
- Request for far-field pattern

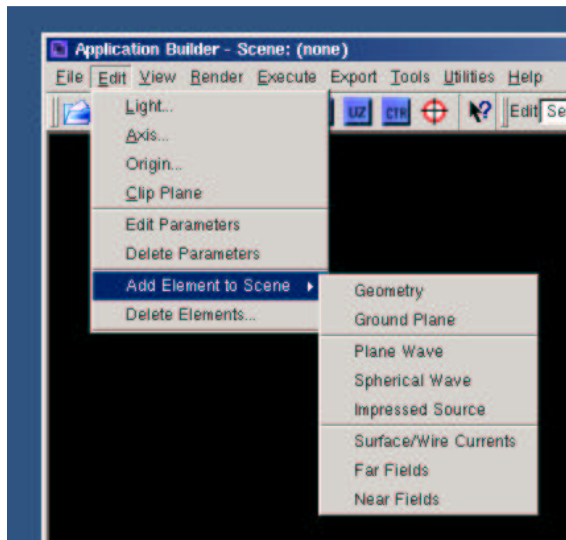


Figure 11. *Application Builder* EM Element List.

The final modeling scene is shown in figure 12. This scenario is exported to GEMACS format, and GEMACS is then executed either within *Application Builder* or separately. The GEMACS results are placed in XML files that will be read by *Component View* for further processing.

### Post-Processing – Component View

*Component View* task-flow maps such as the one shown in figure 13 are used to read the GEMACS geometry and observable results and format them for viewing with SmartView and the other Framework tools.

For example, to produce a visualization of surface currents with the map in figure 13, the *XML Reader* glyph reads the surface current file generated by GEMACS. The *GEMACS Reader* glyph reads the GEMACS geometry structure onto which

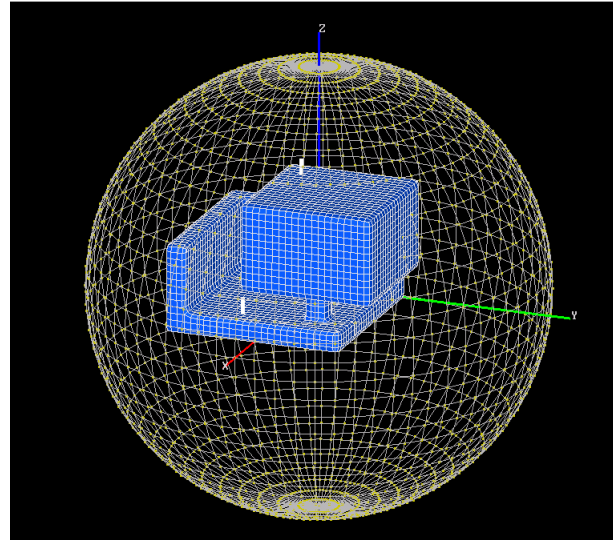


Figure 12. *Application Builder* Screenshot of the Complete Modeling Scenario.

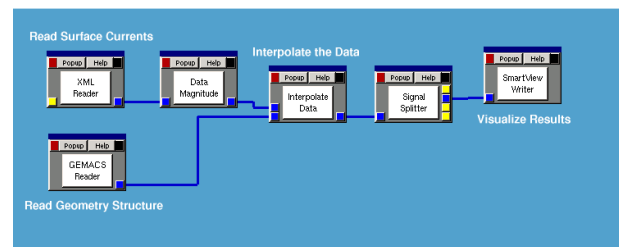


Figure 13. *Component View* Task-Flow Map to Generate Color-Filled Contour Representation of Structure Surface Currents.

the currents are to be mapped. The *Interpolate Data* glyph does the actual work. It assigns the surface current data magnitude to the centers of the corresponding GEMACS surface patches, then interpolates them to the corners of the patches for visualization. Finally, the data passes to the *SmartView Writer* glyph so that we can render it with the *SmartView* tool.

The results of executing this task-flow map are shown in figure 14, where the surface currents have been rendered on a dB scale, with 0 dB corresponding to 0.5 A/m.

The *Component View* map in figure 15 reads the far-field pattern data generated by GEMACS and creates a far-field pattern “surface” as shown in figure 16. Figure 16 has been colorized by pattern intensity, and double-clicking anywhere on the pattern brings up a dialog box that tells the field strength value at that point.

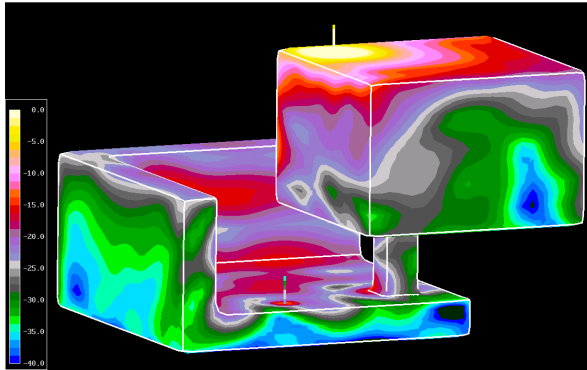


Figure 14. *SmartView* Rendering of Surface Currents When Exciting Antenna #1 (dB Scale).

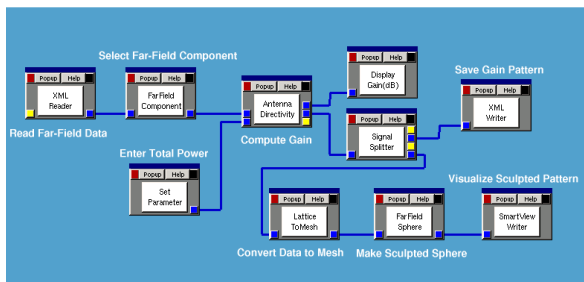


Figure 15. *Component View* Map to Generate the Far-Field Pattern Surface Shown in Figure 16.

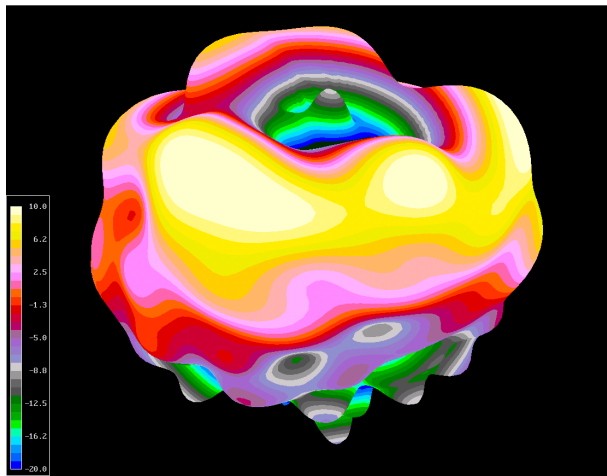


Figure 16. Far-Field Pattern Surface Generated by the *Component View* Map in Figure 15.

While these results are interesting, the design goal was to meet the original specifications over the angular extent stated earlier. We use *Component View* to retain only that part of the pattern in this angular region (figure 17) and then plot its field strength statistically (figure 18).

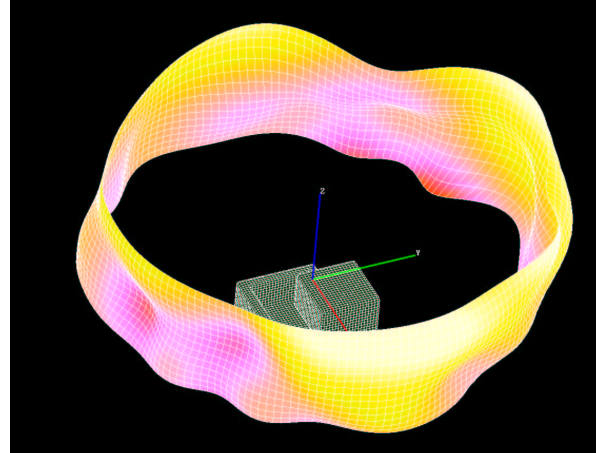


Figure 17. Far-Field Pattern from Antenna #1 Over Angular Region of Interest.

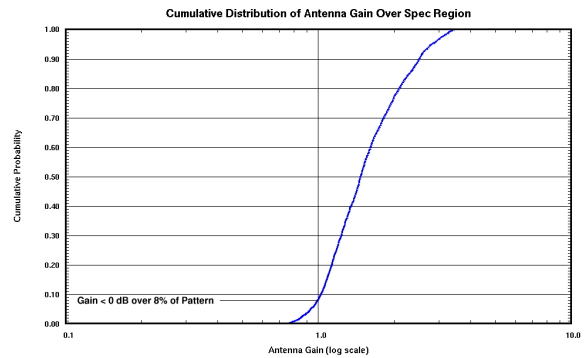


Figure 18. Cumulative Probability Distribution of Far-Field Gain for Antenna #1.

We interpret the statistical results by making the following summary statement:

***“The top-sited antenna will meet the 0 dBi specification over 92% of the specified angular region and fail the specification over 8 of the angular region.”***

Using the Framework tools, it is very simple to repeat the analysis when the lower antenna is excited. Really all that needs to be done is to use *Application Builder* to switch the excitation from the first antenna to the second antenna and repeat

the procedure just outlined. Since the Framework lets the user save and re-use *Application Builder* scenarios and *Component View* maps, generating results from the lower antenna takes only a couple of minutes. When we compare the statistics of the two antennas in figure 19, it is obvious which one is the better choice, for while the top antenna meets the specification 92% of the time, the lower antenna meets it only 46% of the time.

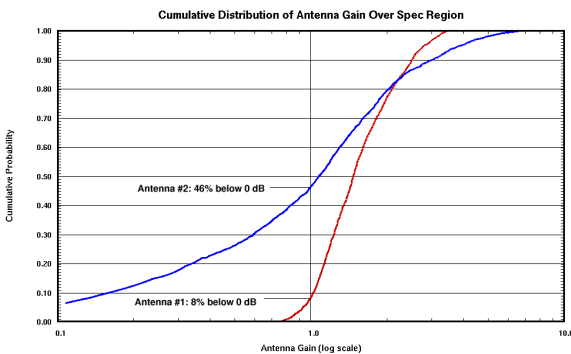


Figure 19. Comparison of Far-Field Pattern CDF's for the Two Candidate Antenna Positions.

Our final conclusion from our EM simulations is this:

***“The top-sited antenna will meet the 0 dBi specification over 92% of the specified angular region, while the lower antenna will meet the 0 dBi specification over only 46% of the specified angular region. We therefore recommend siting the antenna in the upper position”***

## Summary of Results

Generating the results for the first antenna took about 30 minutes, including computer execution time. We saved the *Application Builder* scenario and the *Component View* maps we generated so that they could be re-used for the second antenna.

The results from the second antenna took only about two minutes (plus CEM code execution time) since we were able to re-use the previously saved scenario and task-flow maps.

The statistical comparison of the two antenna patterns provided a method of easily deciding which antenna location was the best one. Moreover, it reduced large amounts of pattern data into a simple statement that could easily be explained to a

non-technical manager tasked to make the final placement decision.

This description of a CEM Framework example within a short article is necessarily terse, but a full description of this example can be found at: <http://www.gemacs.com/ACES/Chapter4.pdf>.

## OTHER APPLICATIONS

This simple example illustrates just a few of the many application areas to which the CEM Framework can be applied. Here are some of the others: Antenna-to-antenna coupling

- EMC/EMI, and EMP
- Cavity field strength contours and surfaces
- Statistical coupling to structures
- Near-zone field contours and surfaces
- Corruption of antenna patterns by obstacles
- Seam, joint, and aperture coupling

## SOFTWARE AVAILABILITY

A CD-ROM and fully functional sixty-day evaluation license are available on request by emailing [support@gemacs.com](mailto:support@gemacs.com), and over 300 copies of the Framework have been distributed this way. The evaluation version does not have printed documentation, but all documentation is on the CD, which you may print yourself or view with the *Help Assistant* tool. Longer evaluation periods are available for users making a more thorough study of the software.

Commercial licensing and support are available from Advanced Electromagnetics. Email [support@gemacs.com](mailto:support@gemacs.com) for details.

## ACKNOWLEDGEMENTS

Sponsorship from the U.S. Army Research Laboratory, U.S. Army Research Office, U.S. Air Force SEEK EAGLE Office, the Naval Surface Warfare Center, and the DoD Joint Spectrum Center is gratefully acknowledged.

## **Surface-Based Integral Equation Formulations for Multiple Material and Conducting Objects**

**Vikram Jandhyala and Swagato Chakraborty**  
**Applied Computational Electromagnetics Laboratory**  
**Dept. of Electrical Engineering, University of Washington**  
**jandhyala@ee.washington.edu**

### **1. Introduction**

The three basic computational approaches that are on the forefront of computational electromagnetics (CEM) are the finite element method (FEM), the finite difference time domain (FDTD) technique, and the method of moments (MoM). The first two techniques, based primarily on the partial differential equation (PDE) form of Maxwell's equations are powerful, reliable, and versatile techniques that are in general use for a variety of EM problems. These are not discussed or summarized in this tutorial except to briefly mention distinctions from the MoM approach.

MoM techniques are based on integral equation (IE) representation of fields and waves derived from Maxwell's equations. These methods have also been in use for several decades now. Unlike FEM and FDTD techniques, which lead to sparse matrices and matrix-free time-stepping respectively, the MoM approach leads to dense matrices based on Green's function interactions.

The MoM is also distinct from the FEM and FDTD in other ways, which can make it particularly suitable for certain classes of EM problems. The MoM in surface formulations only requires discretization of and unknowns placed on surfaces of homogeneous scatterers. This is contrast to PDE based methods where all space including the interior and exterior of scatterers are modeled. Furthermore, these PDE techniques also require truncation of the resulting grids or meshes through artificial absorbing boundary conditions (ABCs).

MoM techniques, in their complete generality, can be used with both volumetric IE formulations and surface IE formulations. This article concentrates on the use of MoM for surface IE formulations, wherein most of the advantages of the MoM are to be found. This tutorial is based on extensive work performed by several outstanding researchers over several decades, and no novelty of treatment is claimed in this article. One of the basic aim of the tutorial is to legitimize the use of surface-based techniques amongst simulation and design engineers who may be more attuned to volumetric techniques where conduction current is an easily understood physical quantity.

We will start with a review of the surface equivalence principle, which is the basic EM principle that enables surface-based IE formulations and resulting MoM. The ideal case of perfect conductors will be discussed as a simple version of this principle. The problem of modeling materials will be then summarized, and extended to multiple finite scatterers.

The important case of lossy conductors, particularly relevant to the microelectronics and emerging nanoelectronics regimes, will be discussed. In addition, a discussion of surface impedance approximations will follow. Finally, results and a discussion will be presented.

It should be pointed that no claim of completeness or wholeness of review is made. The article is based on the authors' necessarily limited viewpoints and experiences, and only supporting and relevant references are provided. Many of the cited works in turn refer to other excellent papers that may not necessarily be cited in this work itself, in addition to other important papers that exist in the extant literature as well.

The MoM formulations presented in this tutorial are implemented using the popular Rao-Wilton-Glisson basis functions. While several advances have been made in higher-order, hierarchical, and other basis functions, these are not in the scope of this article.

## 2. The Surface Equivalence Principle

Surface MoM-based solution of IE forms of Maxwell's Equations are typically based on the surface equivalence principle. This is an important mathematical principle, the existence of which is critical for the correct and exact formulation of MoMs. While this will be discussed again when discussing lossy conductors, it is important to note at the outset that the equivalent surface quantities produced by the application of this principle, and in particular the equivalent surface current, *may not necessarily have a physical meaning such as current flowing on or near a surface*. However, as will be shown, all relevant quantities including, if required, *volumetric conduction current*, can be accurately and exactly recovered, within mesh discretization and related solution error, from post-processing of the MoM system.

We will start with the case of a single homogeneous object (Region 2, with constitutive parameters  $\epsilon_2$  and  $\mu_2$ ) in a (different) homogeneous object (Region 1, with constitutive parameters  $\epsilon_1$  and  $\mu_1$ ). Without loss of generality, it is assumed that the scatterer is excited by a source in Region 1, as shown in Figure 1. The source and its interaction with the scatterer leads to *total* fields  $\mathbf{E}_1$  and  $\mathbf{H}_1$  in Region 1, and  $\mathbf{E}_2$  and  $\mathbf{H}_2$  in Region 2. The

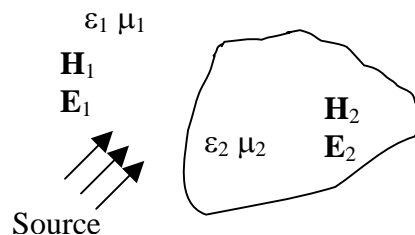


Figure 1: A homogeneous scatterer in a homogeneous medium, excited by an exterior source.

application of the surface equivalence principle in this instance proceeds as follows.

The original problem depicted in Figure 1 is replaced by two *equivalent* problems; the simultaneous solution of these two problems results in the same solution as that of the original problem, in the following sense. As shown in Figure 2, the equivalent exterior problem is constructed by replacing the scatterer by a *mathematical surface* of the same shape, shown with a dotted line. In addition, the entire space interior and exterior to the surface is filled with homogeneous material with constitutive parameters of the original background. It is assumed that in this problem, the correct total fields are produced in the Region 1 exterior to the mathematical surface, and that *zero* fields are produced inside Region 2. Therefore, there are discontinuities of fields across the surface. In order to support this jump, there must exist non-zero electric and magnetic current densities, tangential to the surface,  $\mathbf{J}_1$  and  $\mathbf{K}_1$ . It is important to note that no *physical* meaning should be ascribed to these equivalent current densities; these are merely related to the tangential discontinuities of the fields produced by the mathematical specification of this equivalent problem, through the regular tangential boundary conditions for electric and magnetic fields. In Figure 2,  $\hat{\mathbf{n}}$  represents the outward normal to the surface at any point. Note again that there is no object in this equivalent problem, only a mathematical surface on which exist equivalent current densities, which radiate into a completely homogeneous space. Also note that the original source is present.

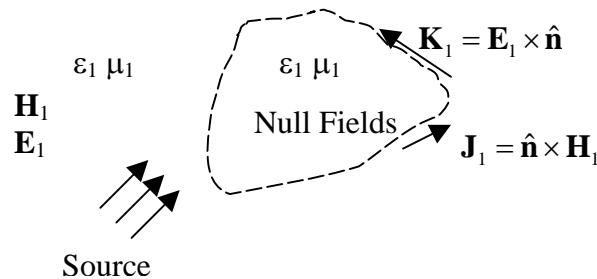


Figure 2: Equivalent exterior problem, with equivalent sources producing the correct total external fields and zero fields interior to the surface bounding the original Region 1.

The second equivalent problem, depicted in Figure 3, is the interior problem. In this case, the entire space is filled with the constitutive parameters of the scatterer.

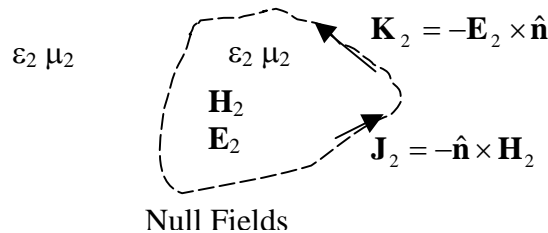


Figure 3: Equivalent interior problem, with equivalent sources producing the correct total internal fields and zero fields exterior to the surface bounding the original Region 1.

In this problem, it is assumed that equivalent current densities  $\mathbf{J}_2$  and  $\mathbf{K}_2$  which support a different discontinuity in the fields across the surface are produced. True fields are produced in the interior of the surface, and zero fields are produced outside. The original source no longer exists in this equivalent problem; however the current densities act as secondary sources producing non-zero fields inside the surface. Also note again that these are equivalent current densities only, not to be ascribed physical meaning, and that there is no object remaining in this problem, only a homogeneous medium.

The two equivalent problems are linked by the fact that the two sets of equivalent currents,  $\mathbf{J}_1, \mathbf{K}_1$  and  $\mathbf{J}_2, \mathbf{K}_2$  are not independent. In Figure 1, if tangentially boundary conditions are enforced across the scatterer surface, one can see that since there are no explicit electric or current source densities, the tangential fields must be continuous. Therefore, from the fact that each of the two equivalent problems generates the true fields on each side of the surface, that the two sets of currents must themselves be equal and opposite i.e.  $\mathbf{J}_1 = -\mathbf{J}_2$  and  $\mathbf{K}_1 = -\mathbf{K}_2$  so that the *true* boundary conditions  $\hat{\mathbf{n}} \times (\mathbf{H}_1 - \mathbf{H}_2) = 0$  and  $\hat{\mathbf{n}} \times (\mathbf{E}_1 - \mathbf{E}_2) = 0$  are enforced. Therefore the two equivalent problems need to be setup and solved simultaneously.

In Figures 2 and 3, it can be seen that the equivalent current densities in the exterior problem are shown to be on the outer side of the equivalent surface, and those in the interior problem are shown to be on the inner side of the surface. These limits can, in terms of limits of singular Green's function integrals as observation points approach the surface from either side, give rise to sign changes in formulations and are therefore important. Also, the fact that the equivalent currents produce null fields in the interior (for the equivalent exterior problem), and in the exterior (for the equivalent interior problem) can be used as a verification of correctness, or degree of accuracy, in MoM implementations. This fact (equivalent currents producing null fields) is termed the extinction theorem.

For the special case of a perfect electric conductor (PEC), which is an ideality that proves to be a useful approximation in several scattering problems, the equivalent problem becomes simpler as shown in Figures 4-6.

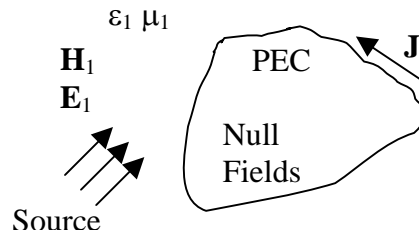


Figure 4: A PEC scatterer

The original scattering situation is shown in Figure 4. There are no fields produced inside the PEC. Also, a true surface current  $\mathbf{J}$  is induced by the source. This current is an actual surface conduction current that exists on an ideal PEC. In addition, the boundary condition that the tangential electric field vanishes on the surface of a PEC needs to be considered. The exterior problem is shown in Fig. 5. Note that all the fields produced by the equivalent source  $\mathbf{J}_1$  are the same as the true fields in Figure 4, including the null fields inside the PEC object of Figure 4. This current radiates in a homogeneous medium with constitutive parameters of Region 1. In this case the equivalent current is identical to the original surface current density  $\mathbf{J}$ ; and the original problem is simply replaced by one where the PEC object is replaced by its surface on which resides the current to be found.

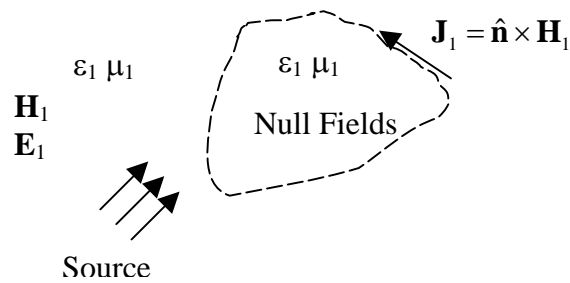


Figure 5: Equivalent exterior problem.

What about the interior equivalent problem? This is shown in Figure 6. This is a *don't care* problem; no current can radiate in a complete PEC background, and hence there is no associated equation to setup or solve.

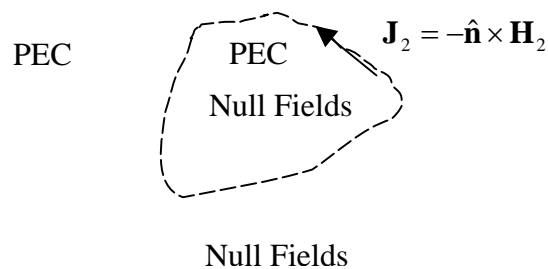


Figure 6: Equivalent interior problem. No radiation occurs in a homogeneous PEC environment.

Note that there are also no equivalent magnetic currents; the fact that the electric field has zero tangential component on the surface of the PEC assures this in the non-trivial exterior problem.

If the PEC is replaced by a finite conductivity metal structure, the exact equivalent problems are significantly different from the PEC case, and resemble the dielectric problem. Figure 7 shows the conductor of conductivity  $\sigma$  and the external source.

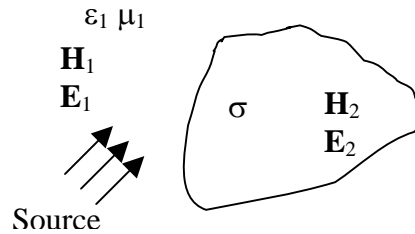


Figure 7: A homogeneous conducting scatterer in a homogeneous medium, excited by an exterior source.

In this case, in the exact formulation, both the exterior and interior problems, shown in Figures 8 and 9 are relevant.

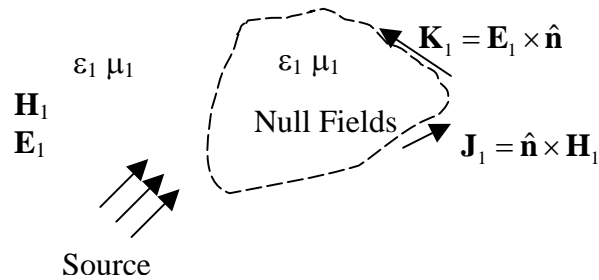


Figure 8: Equivalent exterior problem.

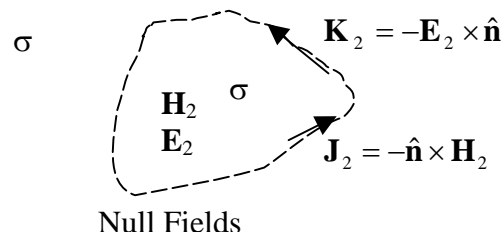


Figure 9: Equivalent interior problem. Currents radiate in a homogeneous region with the conductivity of the original scatterer

In the interior problem, the homogenous material has finite conductivity and is therefore lossy but permits some propagation of fields. As the conductivity increases, this propagation will reduce, and it can be shown that the magnitude of the magnetic current density will drop. The case of finite conductivity will be discussed in more detail later in this paper. Note that unlike the PEC case, the fields interior to the conductor are not assumed to be zero, and that both electric and magnetic current densities are assumed, with no physical properties assigned to these quantities.

Finally, we will now generalize the discussion to an arbitrary number of material objects. If there are  $N$  such objects, there will be  $N+1$  simultaneous equivalent problems. The four equivalent problems for this case are shown in Figures 10-14.

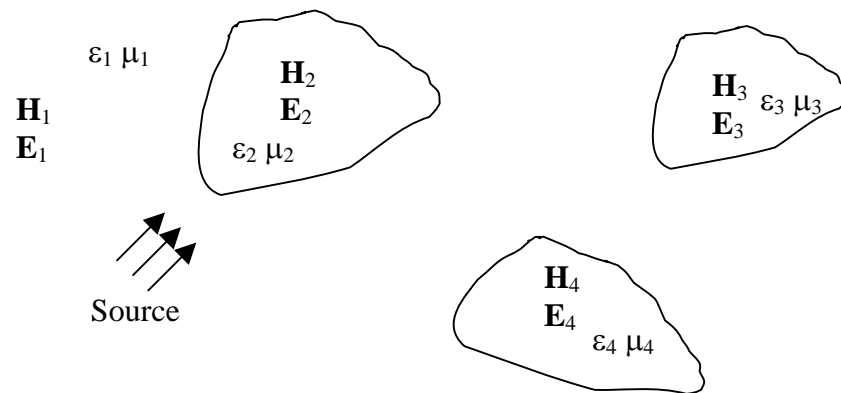


Figure 10: Original multibody problem.

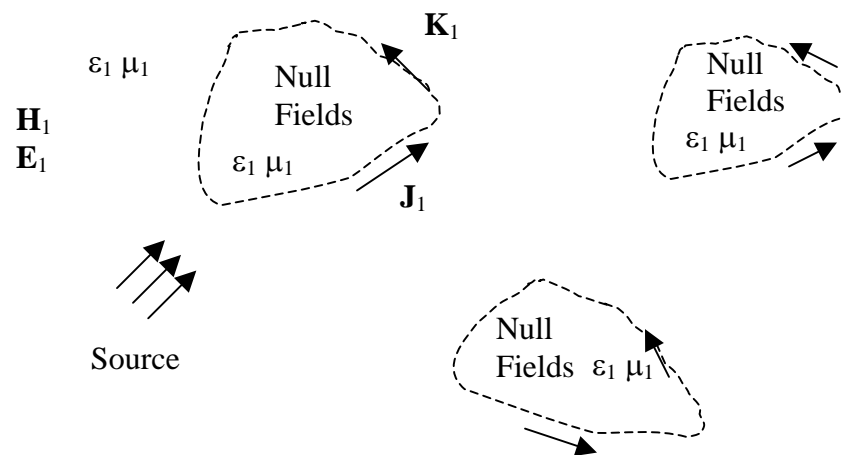


Figure 11: Equivalent problem for Region 1

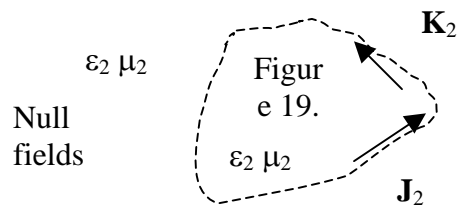


Figure 12: Equivalent problem for Region 2

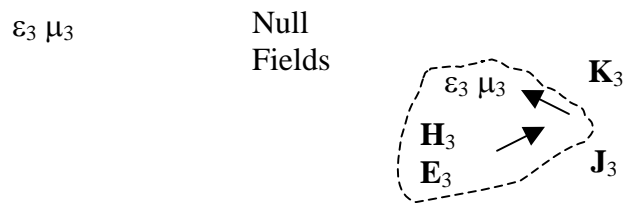


Figure 13: Equivalent problem for Region 3

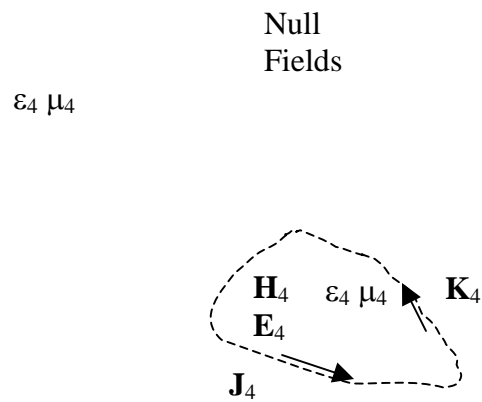


Figure 14: Equivalent problem for Region 4

From Figures 10-14, it is seen that the first equivalent problem includes all surfaces, and equivalent currents are placed on all of them. All the remaining equivalent problems have only one surface associated with them. As in the simpler cases, all these equivalent currents are not independent; they are equal and opposite to the equivalent currents in Figure 10 for each particular surface.

If any of the objects are conducting, the discussion on modeling finite conductivity objects is immediately valid. If any object is a PEC, the interior problem for that object is trivial and can be removed, and no magnetic currents are associated with that surface either in its own equivalent problem or in the first equivalent problem.

### 3. Surface Integral Equations for PEC Scatterers

#### 3.1 Electric Field Integral Equation (EFIE)

The integral equations associated with a PEC scatterer are based on the exterior problem depicted in Figure 5. The total electric field in Region 1 satisfies the boundary condition

$$\mathbf{E}_1(\mathbf{r})\Big|_{\tan} = 0, \mathbf{r} \in S \quad (1)$$

where  $S$  denotes the surface of the PEC scatterer,  $\tan$  represents field quantities tangential to  $S$ , and  $\mathbf{r}$  represents field observation points. If we split the field into an incident part created by the source and a scattered part created by the source interacting with the scatterer through the induced current  $\mathbf{J}$ , we get the condition

$$\mathbf{E}_1^{scat}(\mathbf{r})\Big|_{\tan} + \mathbf{E}_1^{inc}(\mathbf{r})\Big|_{\tan} = 0 \quad (2)$$

where the scattered field is represented in mixed potential form as

$$\mathbf{E}_1^{scat}(\mathbf{r}) = -j\omega\mathbf{A}_1(\mathbf{r}) - \nabla\phi_1(\mathbf{r}) \quad (3)$$

where  $\omega$  is the angular frequency,  $\mathbf{A}$  and  $\phi$  are the magnetic vector potential and electric scalar potential respectively and are obtained by convolution of the Green's function and sources, namely the surface current density  $\mathbf{J}$  and the surface charge density  $\rho$ .

$$\mathbf{A}_1(\mathbf{r}) = \frac{\mu_1}{4\pi} \int_{S'} G_1(\mathbf{r}, \mathbf{r}') \mathbf{J}_1(\mathbf{r}') ds' \quad (4)$$

$$\phi_1(\mathbf{r}) = \frac{1}{4\pi\epsilon_1} \int_{S'} G_1(\mathbf{r}, \mathbf{r}') \rho_1(\mathbf{r}') ds' \quad (5)$$

The Green's function is expressed as follows

$$G_1(\mathbf{r}, \mathbf{r}') = \frac{e^{-jk_1|\mathbf{r}-\mathbf{r}'|}}{|\mathbf{r}-\mathbf{r}'|} \quad (6)$$

where  $k$  is the wave number in the corresponding medium and  $\mathbf{r}$ ,  $\mathbf{r}'$  are the observation and source points respectively. The surface charge density and the surface current density are related by the continuity equation given by

$$\nabla_S \cdot \mathbf{J}(\mathbf{r}) + j\omega\rho(\mathbf{r}) = 0 \quad (7)$$

Putting (7) in (5) we can write (3) as

$$-j\omega \frac{\mu_1}{4\pi} \int_{\mathbf{r}' \in S} G_1(\mathbf{r}, \mathbf{r}') \mathbf{J}_1(\mathbf{r}') ds' - \nabla \frac{j}{4\pi\epsilon_1\omega} \int_{\mathbf{r}' \in S} G_1(\mathbf{r}, \mathbf{r}') (\nabla' \cdot \mathbf{J}_1(\mathbf{r}')) ds' \Big|_{\tan} = -\mathbf{E}_1^{inc}(\mathbf{r}) \Big|_{\tan} \quad (8)$$

At this stage the unknown current density is discretized using basis functions  $\mathbf{f}_i(\mathbf{r})$  scaled by unknown coefficients

$$\mathbf{J}(\mathbf{r}) = \sum_{i=1}^N \alpha_i \mathbf{f}_i(\mathbf{r}) \quad (9)$$

and we test (8) with a tangential testing function  $\mathbf{t}(\mathbf{r})$  to obtain a system of linear equation given by

$$\bar{\mathbf{Z}} \mathbf{I} = \mathbf{V} \quad (10)$$

where ,

$$Z_{mm} = \left\langle \mathbf{t}_m(\mathbf{r}), \left\{ \frac{-j\omega\mu_1}{4\pi} \int_{\mathbf{r}' \in S_n} G_1(\mathbf{r}, \mathbf{r}') \mathbf{f}_{1,n}(\mathbf{r}') ds' \right\} \right\rangle \quad (11)$$

$$+ \left\langle \nabla \cdot \mathbf{t}_m, \left\{ \frac{j}{4\pi\epsilon_1\omega} \int_{\mathbf{r}' \in S_n} G_1(\mathbf{r}, \mathbf{r}') \nabla' \cdot \mathbf{f}_{1,n}(\mathbf{r}') ds' \right\} \right\rangle$$

$$I_n = \alpha_n \quad (12)$$

$$V_m = \left\langle \mathbf{t}_m(\mathbf{r}), -\mathbf{E}_1^{inc}(\mathbf{r}) \right\rangle \quad (13)$$

Typically, Rao-Wilton-Glisson based linear functions are used as both basis and testing functions, though higher order and curvilinear counterparts and multiresolution versions are now becoming increasingly widespread.

### 3.2 Magnetic Field Integral Equation (MFIE)

MFIE is an alternate approach for solving scattering problems where the boundary condition is enforced on the tangential magnetic field behavior across the PEC surface. The jump in the tangential magnetic field across the PEC boundary is supported by a surface current

$$\hat{\mathbf{n}}(\mathbf{r}) \times \mathbf{H}_1(\mathbf{r}) - \hat{\mathbf{n}}(\mathbf{r}) \times \mathbf{H}_2(\mathbf{r}) = \mathbf{J}_1(\mathbf{r}) \quad (14)$$

The magnetic field vanishes inside the PEC scatterer, and just outside the scatterer the total field is decomposed into an incident and scattered field as in (2)

$$\hat{\mathbf{n}}(\mathbf{r}) \times \mathbf{H}_1^{inc}(\mathbf{r}) = \mathbf{J}_1(\mathbf{r}) - \hat{\mathbf{n}}(\mathbf{r}) \times \mathbf{H}_1^{scat}(\mathbf{r}) \quad (15)$$

The scattered magnetic field is expressed in terms of magnetic vector potential as

$$\mathbf{H}_1^{scat}(\mathbf{r}) = \frac{1}{\mu_1} \nabla \times \mathbf{A}_1(\mathbf{r}) \quad (16)$$

Using (4), (15) and (16), and rearranging the order of the differential operator we get

$$\hat{\mathbf{n}}(\mathbf{r}) \times \mathbf{H}_1^{inc}(\mathbf{r}) = \frac{\mathbf{J}_1(\mathbf{r})}{2} + \hat{\mathbf{n}}(\mathbf{r}) \times \frac{1}{4\pi\mu_1} \int_{\mathbf{r}' \in S} \nabla G_1(\mathbf{r}, \mathbf{r}') \times \mathbf{J}_1(\mathbf{r}') ds' \quad (17)$$

Now expanding the unknown current density as in (9) and using the appropriate testing operation, we get a linear system similar to (10), where the matrix elements are given by

$$Z_{mn} = \left\langle \mathbf{t}_m(\mathbf{r}), \frac{\mathbf{f}_{1,n}(\mathbf{r})}{2} \right\rangle + \left\langle \mathbf{t}_m(\mathbf{r}), \left( \hat{\mathbf{n}}(\mathbf{r}) \times \frac{1}{4\pi\mu_1} \int_{\mathbf{r}' \in S_n} \nabla G_1(\mathbf{r}, \mathbf{r}') \times \mathbf{f}_{1,n}(\mathbf{r}') ds' \right) \right\rangle \quad (18)$$

and the right hand side vector is

$$V_m = \left\langle \mathbf{t}_m(\mathbf{r}), -\hat{\mathbf{n}} \times \mathbf{H}_1^{inc}(\mathbf{r}) \right\rangle \quad (19)$$

MFIE is an integral equation of second kind, hence has much better spectral properties and is more suitable for iterative solution. However applicability of MFIE is limited to closed 3D objects owing to the jump condition in the tangential boundary condition.

## 4. Surface Integral Equation for Penetrable Scatterers

### 4.1 Two-region PMCHWT

For non-PEC boundaries the tangential field components do not vanish on or inside the object enclosed by the surface. In that case the boundary conditions on the  $\mathbf{E}$  and  $\mathbf{H}$  fields are

$$\mathbf{E}_1|_{\tan} = \mathbf{E}_2|_{\tan} \quad (20a)$$

$$\mathbf{H}_1|_{\tan} = \mathbf{H}_2|_{\tan} \quad (20b)$$

To model such a problem, we use two equivalent problems, as discussed, the equivalent exterior problem (Fig. 8), and the interior equivalent problem (Fig. 9).

Decomposing the total field into the incident and the scattered field like (2), (15) we get

$$\mathbf{E}_1^{scat} - \mathbf{E}_2^{scat} \Big|_{\tan} = -\mathbf{E}_1^{inc} + \mathbf{E}_2^{inc} \Big|_{\tan} \quad (21a)$$

$$\mathbf{H}_1^{scat} - \mathbf{H}_2^{scat} \Big|_{\tan} = -\mathbf{H}_1^{inc} + \mathbf{H}_2^{inc} \Big|_{\tan} \quad (21b)$$

Now we can express the field quantities in terms of the constituent potentials as follows

$$\left. \begin{aligned} -j\omega \mathbf{A}_1(\mathbf{r}, \mathbf{J}_1) - \nabla \phi_1 \left( \mathbf{r}, \frac{\nabla \cdot \mathbf{J}_1}{-j\omega} \right) - \frac{1}{\varepsilon_1} \nabla \times \mathbf{F}_1(\mathbf{r}, \mathbf{K}_1) + \\ j\omega \mathbf{A}_2(\mathbf{r}, \mathbf{K}_2) + \nabla \phi_2 \left( \mathbf{r}, \frac{\nabla \cdot \mathbf{J}_2}{-j\omega} \right) + \frac{1}{\varepsilon_2} \nabla \times \mathbf{F}_2(\mathbf{r}, \mathbf{K}_2) \end{aligned} \right|_{\tan} = -\mathbf{E}_1^{inc}(\mathbf{r}) + \mathbf{E}_2^{inc}(\mathbf{r}) \Big|_{\tan} \quad (22a)$$

$$\left. \begin{aligned} -j\omega\mathbf{F}_1(\mathbf{r}, \mathbf{K}_1) - \nabla\psi_1\left(\mathbf{r}, \frac{\nabla\cdot\mathbf{K}_1}{-j\omega}\right) + \frac{1}{\mu_1}\nabla\times\mathbf{A}_1(\mathbf{r}, \mathbf{J}_1) + \\ j\omega\mathbf{F}_2(\mathbf{r}, \mathbf{K}_2) + \nabla\psi_2\left(\mathbf{r}, \frac{\nabla\cdot\mathbf{K}_2}{-j\omega}\right) - \frac{1}{\mu_2}\nabla\times\mathbf{A}_2(\mathbf{r}, \mathbf{J}_2) \end{aligned} \right|_{\tan} = -\mathbf{H}_1^{inc}(\mathbf{r}) + \mathbf{H}_2^{inc}(\mathbf{r}) \quad (22b)$$

Here the additional potential quantities, namely the electric vector potential  $\mathbf{F}$ , and the magnetic scalar potential  $\psi$  are given in by the following expressions

$$\mathbf{F}_p(\mathbf{r}, \mathbf{K}) = \frac{\varepsilon_p}{4\pi} \int_{\mathbf{r}' \in S'} G_p(\mathbf{r}, \mathbf{r}') \mathbf{K}_p(\mathbf{r}') ds' \quad (23a)$$

$$\psi_p\left(\mathbf{r}, \frac{\nabla\cdot\mathbf{K}}{-j\omega}\right) = \frac{1}{4\pi\mu_p} \int_{\mathbf{r}' \in S'} G_p(\mathbf{r}, \mathbf{r}') \left(\frac{\nabla\cdot\mathbf{K}_p(\mathbf{r}')}{-j\omega}\right) ds' \quad (23b)$$

where the subscript  $p$  indicates the corresponding medium where the potential is computed. The source  $\mathbf{K}_p$  is the equivalent surface magnetic current radiating in the region  $p$  as described in Fig. (8-9). The unknown electric and magnetic current densities in the interior and the exterior medium are related by a negative sign as discussed. Finally the unknown electric and magnetic surface current densities are expanded as

$$\mathbf{J}(\mathbf{r}) = \sum_{i=1}^N \alpha_i \mathbf{f}_i(\mathbf{r}) \quad (24a)$$

$$\mathbf{K}(\mathbf{r}) = \sum_{i=1}^N \beta_i \mathbf{f}_i(\mathbf{r}) \quad (24b)$$

Following the standard testing operation a linear system similar to (10) is constructed where

$$\bar{\mathbf{Z}} = \begin{pmatrix} \bar{\mathbf{L}}_{EJ} & \bar{\mathbf{M}}_{EK} \\ \bar{\mathbf{M}}_{HJ} & \bar{\mathbf{L}}_{HK} \end{pmatrix} \quad (25)$$

The sub-blocks are linear operators given by

$$\begin{aligned} L_{EJmn} = & \frac{-j\omega}{4\pi} \left\langle \mathbf{t}_m(\mathbf{r}), \left\{ \mu_1 \int_{\mathbf{r}' \in S_n} G_1(\mathbf{r}, \mathbf{r}') \mathbf{f}_{1,n}(\mathbf{r}') + \mu_2 \int_{\mathbf{r}' \in S_n} G_2(\mathbf{r}, \mathbf{r}') \mathbf{f}_{1,n}(\mathbf{r}') ds' \right\} \right\rangle \\ & + \frac{j}{4\pi\omega} \left\langle \nabla \cdot \mathbf{t}_m, \left\{ \frac{1}{\varepsilon_1} \int_{\mathbf{r}' \in S_n} G_1(\mathbf{r}, \mathbf{r}') \nabla' \cdot \mathbf{f}_{1,n}(\mathbf{r}') ds' + \frac{1}{\varepsilon_2} \int_{\mathbf{r}' \in S_n} G_2(\mathbf{r}, \mathbf{r}') \nabla' \cdot \mathbf{f}_{1,n}(\mathbf{r}') ds' \right\} \right\rangle \end{aligned} \quad (26a)$$

$$\begin{aligned} L_{HKmn} = & \frac{-j\omega}{4\pi} \left\langle \mathbf{t}_m(\mathbf{r}), \left\{ \varepsilon_1 \int_{\mathbf{r}' \in S_n} G_1(\mathbf{r}, \mathbf{r}') \mathbf{f}_{1,n}(\mathbf{r}') + \varepsilon_2 \int_{\mathbf{r}' \in S_n} G_2(\mathbf{r}, \mathbf{r}') \mathbf{f}_{1,n}(\mathbf{r}') ds' \right\} \right\rangle \\ & + \frac{j}{4\pi\omega} \left\langle \nabla \cdot \mathbf{t}_m, \left\{ \frac{1}{\mu_1} \int_{\mathbf{r}' \in S_n} G_1(\mathbf{r}, \mathbf{r}') \nabla' \cdot \mathbf{f}_{1,n}(\mathbf{r}') ds' + \frac{1}{\mu_2} \int_{\mathbf{r}' \in S_n} G_2(\mathbf{r}, \mathbf{r}') \nabla' \cdot \mathbf{f}_{1,n}(\mathbf{r}') ds' \right\} \right\rangle \end{aligned} \quad (26b)$$

$$M_{EK\ mn} = \left\langle \frac{\mathbf{t}_m(\mathbf{r})}{4\pi}, \left\{ \frac{1}{\varepsilon_1} \int_{\mathbf{r}' \in S_n} \nabla G_1(\mathbf{r}, \mathbf{r}') \times \mathbf{f}_{1,n}(\mathbf{r}') ds' + \frac{1}{\varepsilon_2} \int_{\mathbf{r}' \in S_n} \nabla G_1(\mathbf{r}, \mathbf{r}') \times \mathbf{f}_{1,n}(\mathbf{r}') ds' \right\} \right\rangle \quad (26c)$$

$$M_{HJ\ mn} = \left\langle \frac{\mathbf{t}_m(\mathbf{r})}{4\pi}, \left\{ \frac{1}{\mu_1} \int_{\mathbf{r}' \in S_n} \nabla G_1(\mathbf{r}, \mathbf{r}') \times \mathbf{f}_{1,n}(\mathbf{r}') ds' + \frac{1}{\mu_2} \int_{\mathbf{r}' \in S_n} \nabla G_1(\mathbf{r}, \mathbf{r}') \times \mathbf{f}_{1,n}(\mathbf{r}') ds' \right\} \right\rangle \quad (26d)$$

The vector of unknowns is given as

$$\mathbf{I} = \begin{bmatrix} \alpha_n \\ \beta_n \end{bmatrix}, n = 1 \dots N \quad (27)$$

,and the right hand side vector is

$$\mathbf{V} = \begin{bmatrix} \left\langle \mathbf{t}_m(\mathbf{r}), \left\{ -\mathbf{E}_1^{inc}(\mathbf{r}) + \mathbf{E}_2^{inc}(\mathbf{r}) \right\} \right\rangle \\ \left\langle \mathbf{t}_m(\mathbf{r}), \left\{ -\mathbf{H}_1^{inc}(\mathbf{r}) + \mathbf{H}_2^{inc}(\mathbf{r}) \right\} \right\rangle \end{bmatrix}, m = 1 \dots N \quad (28)$$

Note that the size of the linear system doubles compared to the PEC problems, as the boundary conditions are on both the electric and the magnetic fields, and the unknowns are the electric and magnetic surface current densities.

## 4.2 Multi-region PMCHWT

The most general configuration consists of an arbitrary number of regions of materials, embedded in a background or free-space. These regions can intersect or touch in general. The approach is to use M+1 surface equivalent problems for M regions (and 1 background region). Then, appropriate boundary conditions (tangential E and H fields), and appropriate identification of independent currents are used to set up the overall equation. The following conditions are used to set up the equations:

- For an interface between a dielectric and a PEC region, the tangential electric field is zero, no equation is present for the tangential magnetic field, the exterior of the PEC has only electric current, and the interior of the PEC does not have any associated unknowns
- For an interface (regions i and j) between two dielectrics or poor conductors,  $\mathbf{J}_i = -\mathbf{J}_j$ ,  $\mathbf{K}_i = -\mathbf{K}_j$ ,  $\mathbf{E}_i = \mathbf{E}_j$ , and  $\mathbf{H}_i = \mathbf{H}_j$
- For an interface between a dielectric and conductor, or between two dissimilar conductors,  $\mathbf{J}_i = -\mathbf{J}_j$ , and  $\mathbf{E}_i = \mathbf{E}_j$
- Boundary conditions and dependence of the basis functions as described above enforced by a sparse, bipolar matrix  $\mathbf{P}_{M \times N}$ , where M is the number of independent basis functions and N is the number of all basis functions combining individual regions.

The system of linear equations thus obtained is presented by

$$\bar{\mathbf{P}}_{M \times N}^T \bar{\mathbf{Z}}_{N \times N} \bar{\mathbf{P}}_{N \times M} \mathbf{I}_M = \bar{\mathbf{P}}_{M \times N}^T \mathbf{V}_N \quad (29)$$

Where  $\bar{\mathbf{Z}}$  is a region by region PMCHWT matrix similar to (25), except that the entries correspond only to a single region rather than the sum of the contributions from two regions.

Pictorially, the matrix equation can be represented as:

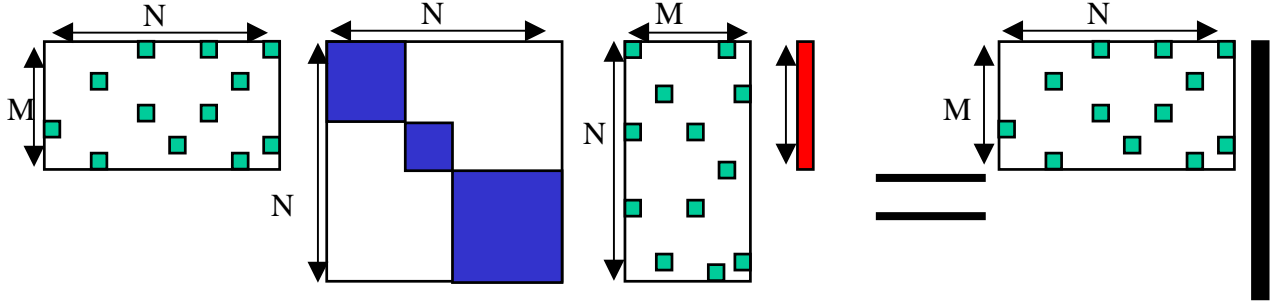


Figure 15: Pictorial representation of the multiregion PMCHWT system matrix

The Green elements are 1's or -1's, the rest of the rectangular matrix contains zeroes, the blue dense portion of the MoM matrix represents interactions within each region, using the Green's function for that region. The red vector is the set of independent electric and magnetic currents, and the long black vector is the set of incident fields.

It is important to take care of the junction problem while handling more than two touching dielectric regions. This is achieved by identify the independent basis function(s) corresponding to the junction and also to set up the corresponding  $\bar{\mathbf{P}}$  matrix entries for the associated dependent basis functions. We do not discuss junctions in any detail here.

## 5. Surface Integral Equation for Lossy Scatterers

For boundary enclosing a region with finite conductivity, the tangential electric field does not vanish on the surface, hence there exists a magnetic current on the boundary and the problem can in general be modeled using PMCHWT equations as described in section 4. The wave number for a conducting medium is given by

$$k = \omega \sqrt{\mu \epsilon_0 \left( 1 + \frac{\sigma}{j\omega \epsilon_0} \right)} \quad (30)$$

where  $\sigma$  is the conductivity of the region. For highly conducting regions, the wave number has a strongly negative imaginary part, so the corresponding Green's function (6) is associated with a very sharp decay which corresponds to the loss in the medium. When the decay becomes very sharp, i.e. for the case of very high conductivity and very high frequency the interior medium Green's function looks like a delta function, and in the limiting case the electric field contribution of the current in the interior medium can be represented locally by a linear term as

$$\mathbf{E}_2 = Z_S \mathbf{J}_2 = (1 + j) \sqrt{\frac{\mu\omega}{2\sigma}} \mathbf{J}_2 \quad (31)$$

$Z_S$  has been described in the literature as the surface impedance, and can be used to simplify the PMCHWT formulation using an impedance boundary condition (IBC) for the restricted case of high conductivity and high frequency. The IBC imposes a local relationship between the surface electric and magnetic current as

$$\mathbf{K} = -Z_S \hat{n} \times \mathbf{J} \quad (32)$$

However, as mentioned before the IBC is a simplification that is applied only to the cases involving high frequency and high conductivity. Whereas a complete two region PMCHWT formulation is general in terms of its applicability to lower frequencies and conductivities, and automatically reduces to IBC at higher frequencies. The Green's function convolution involving highly decaying kernels for conducting media can be handled using specially designed semi-analytic quadrature routines using polar coordinate system.

The surface based technique for modeling loss in conducting structures is useful to evaluate the actual volumetric current flow through the conductor cross-section. The system of linear equations as described in (25-28) is solved to obtain the distribution of equivalent electric and magnetic current on the conductor surface. The surface currents can be post-processed to find the true electric field distribution in the interior of the conductor using the interior medium Green's function as depicted in figure 9. Finally the true volumetric current inside the conducting region  $\mathbf{J}_{vol}$  is obtained as

$$\mathbf{J}_{vol}(\mathbf{r}) = \sigma \mathbf{E}_2(\mathbf{r}) \quad (33)$$

where  $\mathbf{E}_2$  is the interior medium electric field, computed using the interior medium material properties and the equivalent surface electric and magnetic current in the interior region.

*The overall impact of such an approach is a purely surface formulation that correctly captures the volumetric effects including conduction current distribution.*

## 6. Sample Results

Several excellent papers in the literature present exhaustive results using surface based PEC and dielectric MoM formulations. Here, we present some results related to the use of the surface MoM for conducting media, an approach that is occasionally misunderstood with the assumption that some surface approximation to the true conduction current is being enforced. As discussed in the previous sections, this is of course not true as explained through the surface equivalence principle, but this will also be shown through some examples.

Also, all examples shown here are produced using the PILOT code suite, an MoM-based code developed at the Applied Computational Electromagnetics Lab, University of Washington. This integrated code suite includes both surface and hybrid surface-volume formulations, special quadrature for lossy media, circuit interconnectivity and SPICE models, fast frequency sweeps, fast multilevel multipole and rank-compression

algorithms, and multi-stage loop-tree and approximate inverse preconditioners, with algorithms parallelized for multi-processor and workstation clusters.

The first example, in Figure 16 shows a Copper inductor of dimensions  $200\ \mu\text{m} \times 200\ \mu\text{m}$  and metal width  $20\ \mu\text{m}$  over a substrate of height  $100\ \mu\text{m}$ . The substrate has a conductivity of  $1 \times 10^5\ \text{S/m}$ . The MoM code with lossy conductor modeling is used to obtain the quality factor of the inductor. The extremely low peak value of  $Q$  is typical of non-optimized on-chip inductors over lossy substrates, although the low  $Q$  is exaggerated here because of the high conductivity substrate.

The second example, in Figures 17 and 18, shows the extracted inductance and resistance of a Copper bar of dimension  $0.5\text{mm} \times 0.5\text{mm} \times 5\text{mm}$ , and conductivity  $5.8 \times 10^7\ \text{Sm}^{-1}$ . The limiting values of inductance at low and high frequency match against commercial solver, and the expected “S” shaped curve for inductance is obtained with the lossy medium, but not with a simplistic surface impedance approximation. For simple structures like a single bar, the quasi-static resistance can be computed analytically from the skin depth at a given frequency. The analytic resistance exhibits (Figure 18) a close match with the simulation result including the low frequency level-off to the DC resistance, *from a surface-only formulation*. For higher frequencies, the surface impedance results match with the PMCHWT results. However for lower frequencies, the surface impedance based model fails to capture the level-off of the resistance and the inductance curves, that arise due to uniform current flow through the conductor cross-section. The true lossy medium surface formulation captures all relevant resistance effects including near DC.

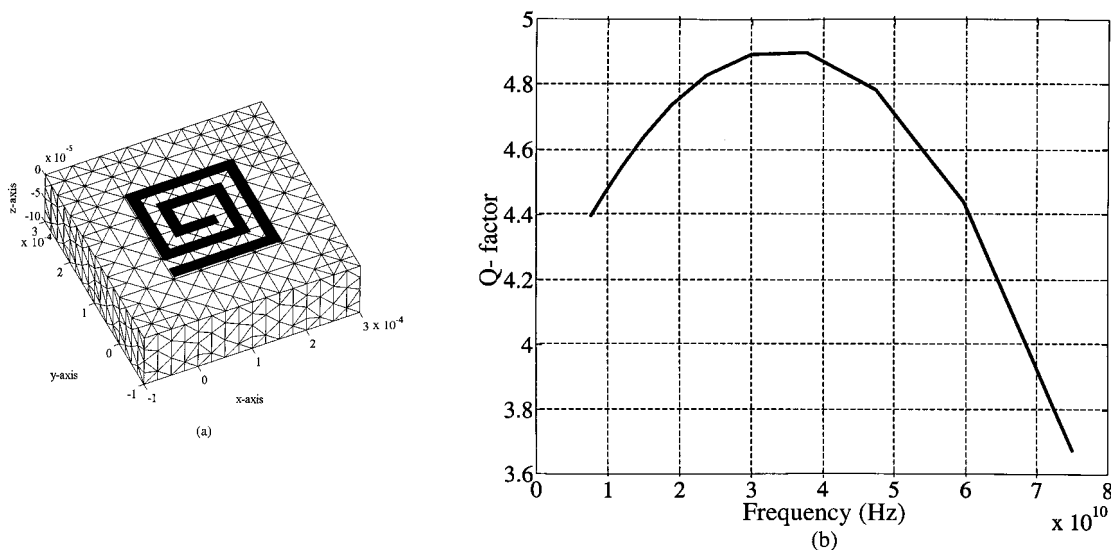


Figure 16: Quality factor of an on-chip spiral inductor on a conducting substrate.

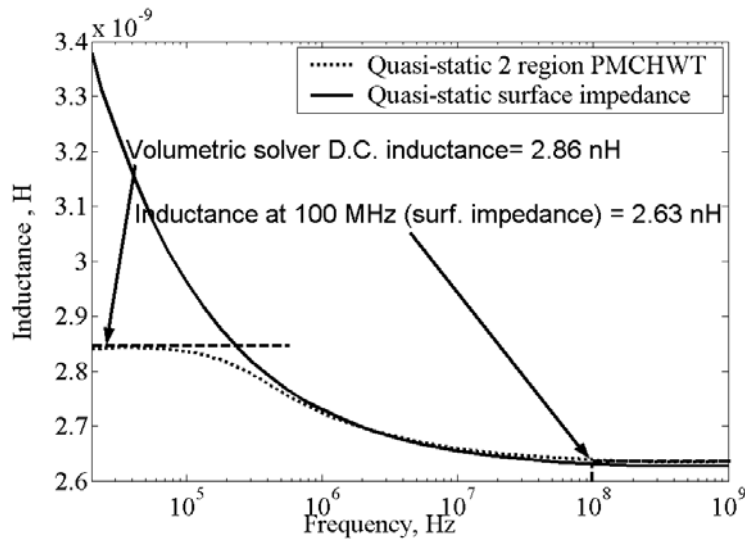


Figure 17: Frequency variation of inductance of a Copper bar using a lossy medium PMCHWT surface formulation

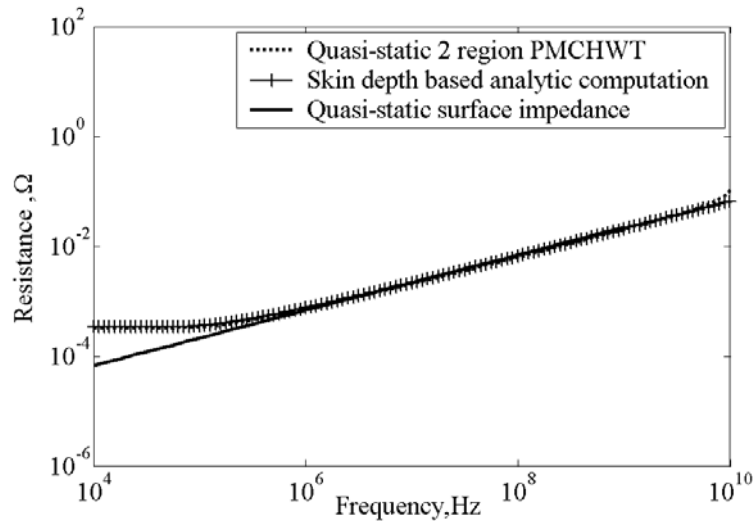


Figure 18: Frequency variation of resistance of a Copper bar using a lossy medium PMCHWT surface formulation.

The next example examines the volumetric current density within a metallic square cross section conductor, captured by post-processing fields obtained from a surface-only formulation. Increasing skin effect in a conductor can happen by changing frequency or conductivity. The case of changing conductivity is shown; as conductivity is increased, the volumetric current attempts to flow near the surface. The same effect can also be shown by plotting, on a log-scale, the fall off of volumetric current away from the surface of the conductor. The numerical value obtained from the surface formulation compares

favorably to the drop-off predicted by an analytic skin-depth approximation, as shown in Figure 20.

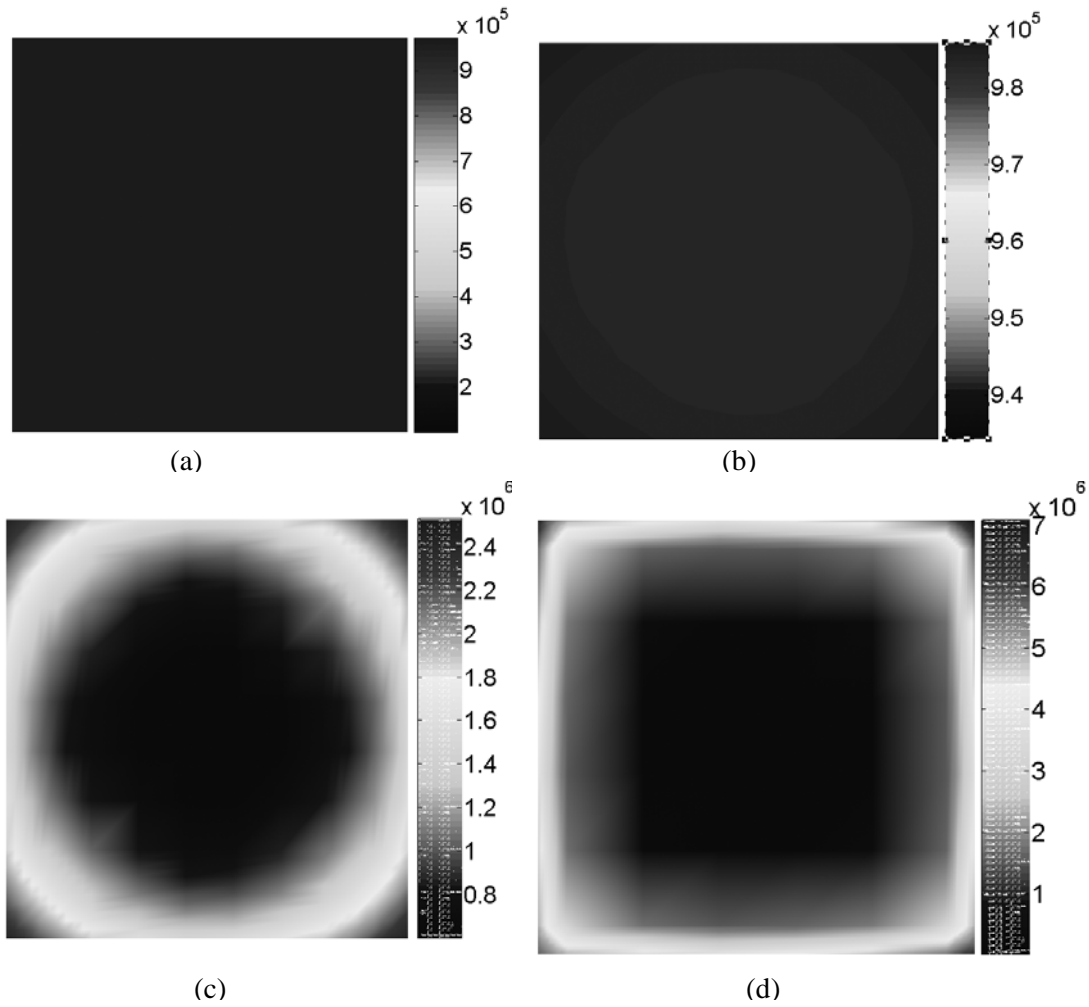


Figure 19. Current distribution in the cross section of a square conductor, with the following ratios of minimum to maximum volumetric current for given conductivities

- (a)  $\frac{J_{\min}}{J_{\max}} = 0.99, \text{freq.} = 1\text{MHz}, \sigma = 5.8 \times 10^4$
- (b)  $\frac{J_{\min}}{J_{\max}} = 0.52, \text{freq.} = 1\text{MHz}, \sigma = 5.8 \times 10^5$
- (c)  $\frac{J_{\min}}{J_{\max}} = 0.1037, \text{freq.} = 1\text{MHz}, \sigma = 5.8 \times 10^6$
- (d)  $\frac{J_{\min}}{J_{\max}} = 0.0009, \text{freq.} = 1\text{MHz}, \sigma = 5.8 \times 10^7$

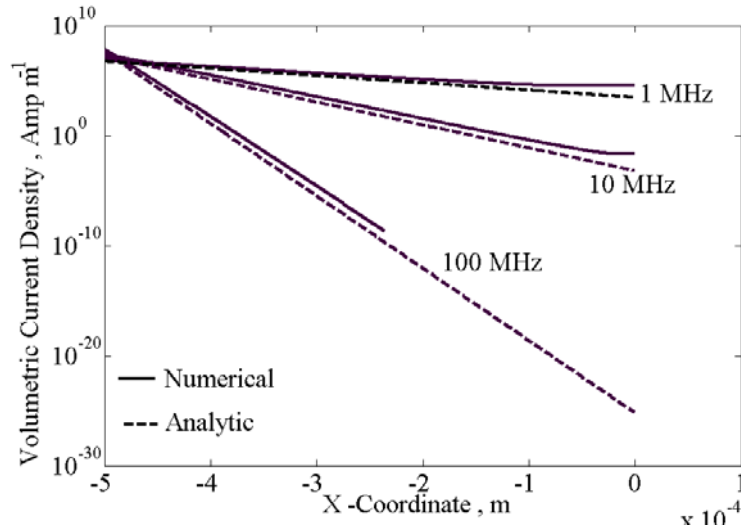


Figure 20. Variation of volumetric current density with the distance from the surface ( $x = -0.5\text{mm}$ ) of a copper conductor with uniform cross section of  $1\text{mm} \times 1\text{mm}$ . The rate of decay is compared against the rate computed from the analytic expression of skin depth for a given frequency and conductivity.

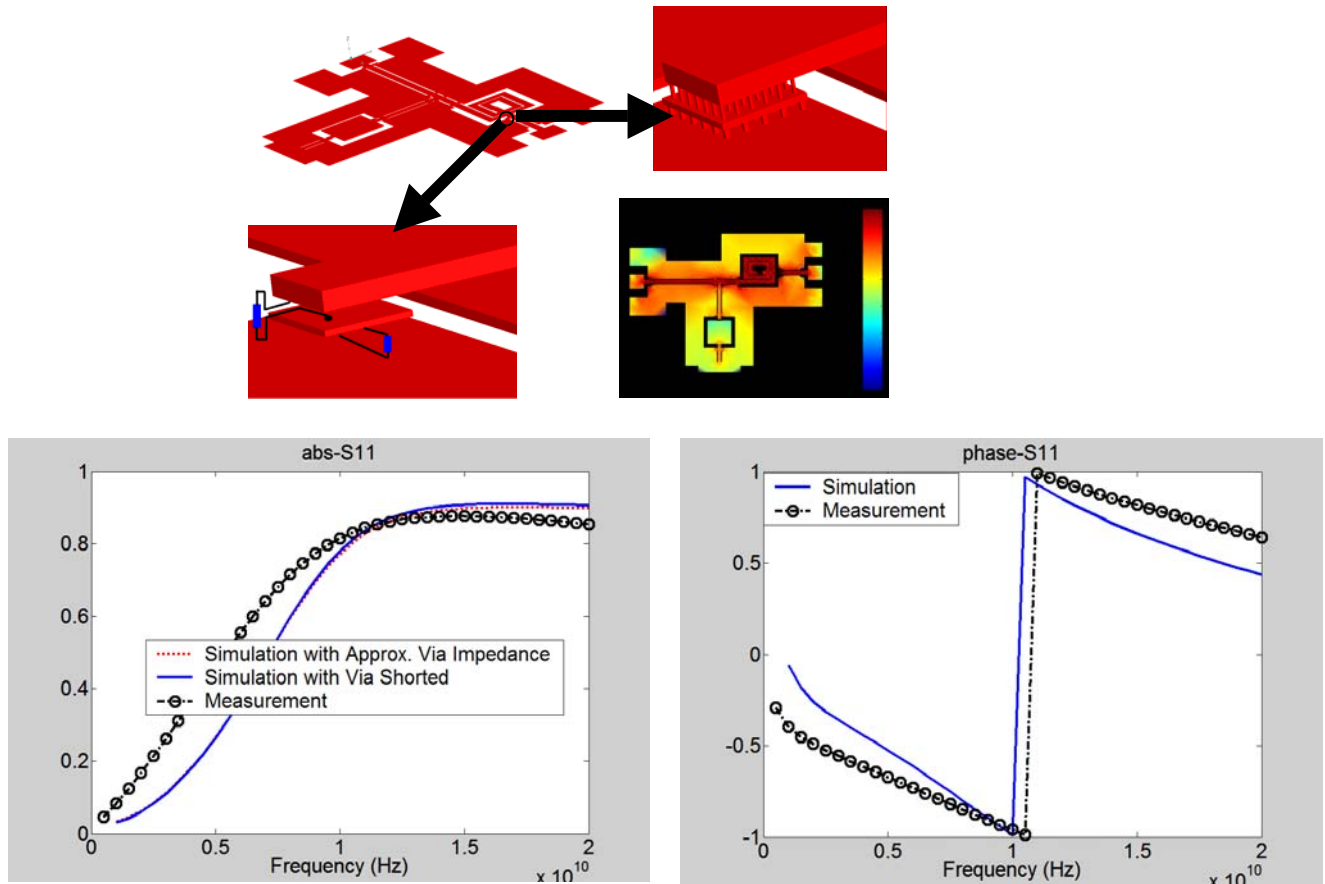


Figure 21: Top: Analog circuit layout, including details of vias and lumped circuit approximations, and current density obtained at 1GHz. Bottom: S-parameters and comparison to measurement.

Finally, the complete power of a surface-based, accelerated MoM solver (PILOT in this case) is shown as in the case of a 4 layer analog sub-circuit that includes a multi-layer inductor, vias, capacitor, coplanar waveguides, and waveguide tees. The entire simulation, completed over the entire frequency band shown in the results, required 15 minutes on a single PC.

## 7. Discussion

This article presented a review of surface-only MoM formulations starting with a summary of surface equivalence principle examples. The case of conducting media was also discussed in particular. Several critical parts of a real-world, powerful MoM code such as PILOT, such as fast multilevel solvers and frequency sweeps, low-frequency conditioning and preconditioning, numerical quadrature, and parallelization have not been discussed in this article. The main aim was to summarize the power, generalization and completeness of surface formulations as developed by a host of excellent researchers. It should be pointed out that there are certainly instances where hybrid surface-volume formulations, or FEM/FDTD formulations, are better suited owing to conditioning issues. In the final analysis, a truly adaptive hybrid code with all these features as well as time and frequency versions, functioning seamlessly with other multi-physics engines, would be a desirable goal within CEM!

## 8. Acknowledgements

The authors would like to thank Drs. Dipanjan Gope and Yong Wang, and graduate students Chuanyi Yang, Gong Ouyang, Indranil Chowdhury, James Pingenot, and Todd West who have all contributed to MoM development at the ACE Lab. Funding from DARPA, NSF, SRC, INTEL, ANSOFT, NASA, Lawrence Livermore National Labs, and the University of Washington is gratefully acknowledged.

## 9. Bibliography

The following is a set of excellent papers, but is by no means exhaustive.

[1] R. F. Harrington, *Field Computation by Moment Methods*, Krieger publishing Co., Malabar, Florida, pp. 71-72,1982.

[2] S. M. Rao, D. R. Wilton and A. W. Glisson, "Electromagnetic scattering by surfaces of arbitrary shape," *IEEE Trans. on Antennas and Propagation*, vol. 30, pp. 409-418, May 1982.

[3] D. Wilton, S. Rao, A. Glisson, D. Schaubert, O. Al-Bundak and C. Butler, "Potential integrals for uniform and linear source distributions on polygonal and polyhedral

domains, ”*IEEE Trans. on Antennas and Propagation*, vol. 32(3), pp. 276 -281, Mar. 1984.

[4] J.S. Zhao and W.C. Chew, “Integral equation solution of Maxwell's equations from zero frequency to microwave frequencies,” *IEEE Trans. on Antennas and Propagation* vol. 48(10), pp. 1635-1645, Oct. 2000.

[5] Umashankar, A.Taflove and S.Rao, “Electromagnetic scattering by arbitrary shaped three-dimensional homogeneous lossy dielectric objects,” *IEEE Trans. on Antennas and Propagation*, vol. 34(6), pp. 758-766, Jun 1986.

[6] A.J. Poggio, E.K. Miller, Y. Chang, R.F. Harrington, T.K Wu and L.L. Tsai. PMCHWT combined integral equation formulation named after the contributors, 1973-1977. Original collective work.

[7] B.M. Kolundjiza, “Electromagnetic modeling of composite metallic and dielectric structures,” *IEEE Trans. On Microwave Theory and Tech.* vol. 47(7), pp. 1021-1032, Jul. 1999.

[8] P.M. Goggans, A.A. Kishk and A.W. Glisson, “Scattering from conductors coated with materials of arbitrary thickness,” *IEEE Trans. Of Antennas and Propagation.* vol. 40(1), pp. 108-112, Jan. 1992.

[9] S. Chakraborty and V.Jandhyala, “Evaluation of Green’s Function Integrals in Conducting Media,” *IEEE Trans. on Antennas and Propagation*, vol. 52(12), pp. 3357-3363, Dec 2004.

[10] T.K Sarkar, E. Arvas,.S. Ponnappalli, ” Electromagnetic Scattering From Dielectric Bodies,”*IEEE Trans. on Antennas and Propagation*, vol. 37(5),pp. 673 – 676, May 1989.

[11] T.K. Wu and L.L.Tsai, “Scattering from arbitrarily-shape lossy dielectric body of revolution,” *Radio Sci.* , vol. 12(5), pp. 709-718, 1977.

[12] A. E. Ruehli, “Equivalent circuit models for three-dimensional multiconductor systems,” *IEEE Trans. Microwave Theory and Techniques*, vol. 22(3), pp. 216-221, March 1974.

[13] J. Jin, “The Finite Element Method in Electromagnetics,” *New York: John Wiley & Sons*, 1993.

[14] A. Taflove, "Computational Electrodynamics: The Finite-Difference Time-Domain Method," *Boston Artech House*, 1995.

[15] T. Sarkar , S. Rao, A. Djordjevic, "Electromagnetic scattering and radiation from finite microstrip structures," *IEEE Trans. on Microwave Theory and Techniques*, vol. 38(11), pp. 1568 – 1575, Nov. 1990.

[16] D. Schaubert, D. Wilton, A. Glisson, "A tetrahedral modeling method for electromagnetic scattering by arbitrarily shaped inhomogeneous dielectric bodies," *IEEE Trans. on Antennas and Propagations*, vol. 32(1), pp. 77-85, Jan 1984.

[17] W.C. Chew, J.M. Jin, E. Michielssen and J. Song, "*Fast Efficient Algorithms in Computational Electromagnetics*," Artech House, Boston, London 2001.

[18] A. W. Glisson, "Electromagnetic scattering by arbitrarily shaped surfaces with impedance boundary conditions," *Radio Science*, vol. 27(6), pp. 935-943, Nov. 1992.

[19] S. Chen, J. S. Zhao, and W. C. Chew, " Analyzing low-frequency electromagnetic scattering from a composite object," *IEEE Trans. on Geoscience and Remote Sensing*, vol. 40(2), pp. 426-433 , Feb. 2002.

[20] J.M Putnam and , L.N. Medgyesi-Mitschang, "Combined field integral equation formulation for inhomogeneous two and three-dimensional bodies: the junction problem," *IEEE Trans. on Antennas and Propagation*, vol. 39(5), pp. 667 – 672, May 1991.

[21] J.R.Mautz and R.F. Harrington, "A combined-source solution for radiation and scattering from a perfectly conducting body," *IEEE Trans. on Antennas and Propagation*, vol.27, pp-445-454, 1979.

[22] T.K Sarkar, B. Kolundjiza, A.R. Djordjevic and M. Salazar-Palma, "Accurate modeling of frequency responses of multiple planes ingigahertz packages and boards," *IEEE Conference on EPEP*, pp. 59-62, 2000.

[23] J.Wang, J. Tausch, and J. White, "A wide frequency range surface integral formulation for 3-D RLC extraction," in *Dig. Technical Papers Int. Conf. Computer-Aided Design*, pp. 453–457,Nov. 1999.

[24] A. W. Glisson, "Electromagnetic scattering by arbitrarily shaped surfaces with impedance boundary conditions," *Radio Sci.*, vol. 27(6), pp. 935–943, Nov. 1992.

[25] A. W. Glisson, "An integral equation for electromagnetic scattering by homogeneous dielectric bodies", *IEEE Trans. on Antennas and Propagation*, vol. 32, pp. 173-175, Feb. 1984.

[26] T.K. Sarkar, E. Arvas and S. Ponnappalli, "Electromagnetic scattering from dielectric bodies," *IEEE Trans. on Antennas and Propagation*, vol. 37(5), pp. 673-676, May 1989.

[27] R. Mittra, and D. R. Wilton, "A numerical approach to the determination of electromagnetic scattering characteristics of perfect conductors," *Proceedings of the IEEE*, vol. 57(11), pp. 2064 – 2065, Nov. 1969.

[28] C.C. Lu and W.C. Chew, "A coupled surface-volume integral equation approach for the calculation of electromagnetic scattering from composite metallic and material targets," *IEEE Transactions on Antennas and Propagation*, vol. 48(12), pp. 1866 – 1868, Dec. 2000.

[29] T.E. Van Deventer.; P.B. Katehi and A.C. Cangellaris, "An integral equation method for the evaluation of conductor and dielectric losses in high-frequency interconnects," *IEEE Transactions on Microwave Theory and Techniques*, vol. 37(12), pp. 1964 – 1972, Dec 1989.

# A BROADBAND DOUBLE RIDGE GUIDE HORN WITH IMPROVED RADIATION PATTERN

Vicente Rodriguez  
ETS-Lindgren, L.P.  
1301 Arrow Point Dr  
Cedar Park, TX 78613  
[Vince.Rodriguez@ets-lindgren.com](mailto:Vince.Rodriguez@ets-lindgren.com)

*Abstract.*- Broadband antennas are the workhorse of EMC testing and Antenna Pattern Measurement. The large frequency band allows testing of equipment without interruptions to change antennas. Until recently the main antenna parameter of interest to the EMC engineer was the antenna factor (AF). EMC engineers were not interested in antenna patterns, most antennas were assumed to have a directive pattern with a smooth main lobe. As testing at higher frequencies has become important, attention to the radiation pattern has become a key issue. Recently a double ridge guide horn (DRGH) design has been found to have a very poor pattern for about half of the band it covers. This traditional design has been accepted in the EMC community as a standard antenna. In the paper a new design of DRGH is introduced which maintains a single lobe radiation pattern over the entire band and is comparable in gain and AF with the traditional design.

**Key words:** EMC, Antennas, time domain methods.

## I. Introduction

There are two main types of radiated EMC measurements; Radiated Immunity or Susceptibility and Radiated Emissions. Antennas are used in radiated EMC testing to sense and generate fields. International and national standards define the test distance, antenna to be used and location of the equipment [1]. For years the EMC engineer paid little attention to the pattern of the antenna being used. The EMC engineer would have an idea of the direction of the main beam and would point the antenna to the equipment under test (EUT) so that this fell under the main beam. Originally most Standards called for the use of half-wavelength dipoles for frequencies 80MHz and higher and for short dipoles for frequencies below 80MHz. However, in order to reduce test time broadband antennas such as bi-conical dipoles and log periodic dipole arrays began to be accepted. The use of broadband antennas reduced the test time since the technician did not have to stop the test and adjust or change the dipole antenna for the next short band of frequencies. As the use of broadband antennas extended standards were changed to allow for the use of broadband antennas as long as the measurements performed with these antennas could be related to the half wave dipole. Other Standards went further and defined which broadband antennas must be used. The latest version of the Military Standard Mil-Std 461E stated the use of broadband DRGH as the antenna of choice for frequencies above 200MHz [2].

One of the antennas required by [2] was a DRGH for the 1GHz to 18GHz range. This broadband horn has been an accepted antenna in EMC for over 40years. On February 2003 a paper appeared [3] that showed the numerical analysis of a traditional 1-18GHz DRGH commonly used in EMC measurements. The authors pointed out deficiencies in the pattern that in their view rendered the antenna use in EMC applications as questionable.

These revelations in [3] were not a surprise to most users, especially those using the antenna for susceptibility. In susceptibility or immunity testing the antenna must generate a uniform field over a given vertical plane. These users knew of the problems for the traditional 1-18GHz antenna to effectively illuminate the 1.5m by 1.5m uniformity plane. Figure 1 shows the measured pattern of the traditional design at 16GHz showing the main beam broken into 5 smaller lobes.

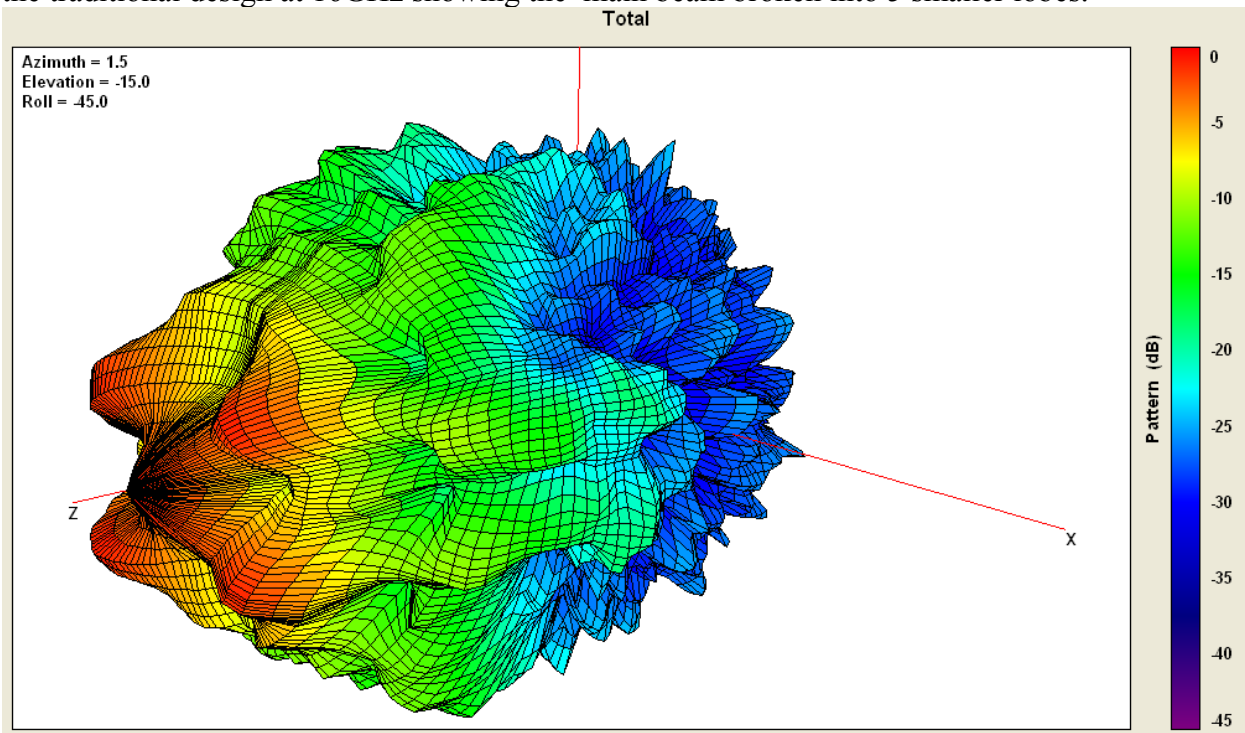


**Figure 1. The 3D measured pattern of the traditional Double-ridged guide horn.**

This paper presents an improved design of the 1-18GHz DRGH. The new antenna maintains a single radiation lobe for the entire frequency range. As in reference [3] the entire horn was modeled, including the coaxial feed. Additionally, prototypes of the antenna were manufactured and tested and the results compared with the model predictions. The improvement was based on applying different ideas to the horn and making sure that the propagation of higher order modes was suppressed.

A time domain method was chosen for the analysis. CST Microwave Studio was the commercial solver chosen to design the new antenna.

## II. Numerical Analysis

The antenna is modeled as a PEC structure fed by a coaxial line with 50 ohm impedance. A PMC symmetry plane is used so that it is only needed to solve half of the geometry. Figure 2 shows the geometry generated in the numerical model.

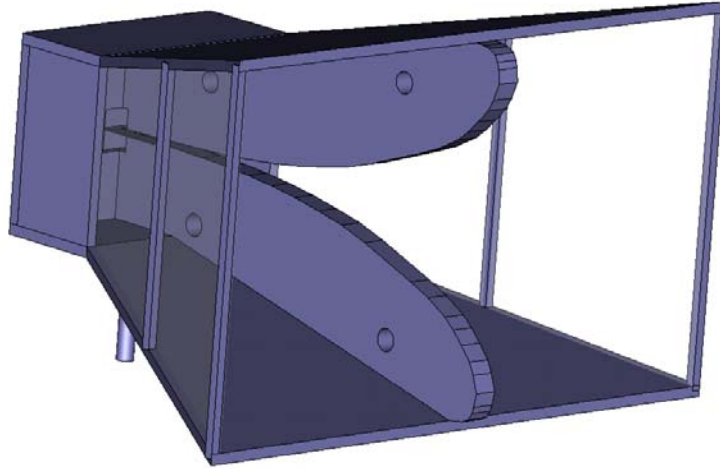


Figure 2. The original model of the new DRGH.

The starting point of the design was to model the traditional DRGH design as it was done in [3]. From this analysis several modifications were adopted. First the new antenna was reduced in size to push to higher frequencies the split pattern problem. Additionally the feed cavity was redesigned. Figure 3 shows the new feed cavity showing a structure design to suppress higher order modes. Also the curvature of the ridges was changed to achieve better matching at the aperture of the horn.



Figure 3. The feed cavity of the new DRGH for EMC applications.

The results from the analysis showed that the side-bars were increasing the gain at the low frequencies as reported in [3]. Additionally, it was found that the dielectric supports for these bars were having a detrimental effect on the main beam at the higher end of the range. The final design

was implemented without any sides. Mechanically no additional support was needed for the top and bottom plates. Figure 4 shows the final geometry being analyzed.

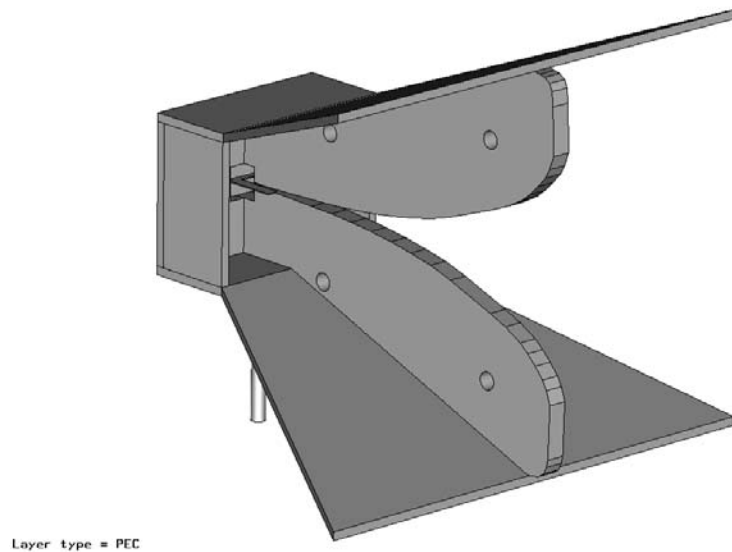


Figure 4. The final geometry of the new DRGH for EMC testing.

### III. Numerical Results and Measurements.

The results from the numerical model that were of interest to the design goals were the directivity or directive gain (which is related to the AF), the VSWR and the radiation pattern quality. The objective was to get an antenna with similar performance to the traditional design but with better pattern behavior.

Once the numerical model design was finalized three prototypes were manufactured. Figure 5 shows one of the 3 prototypes.



Figure 5. One of the three prototypes of the new antenna.

The VSWR, gain and pattern of the prototypes were measured. Figure 6 shows the VSWR of the model compared to the 3 prototypes.

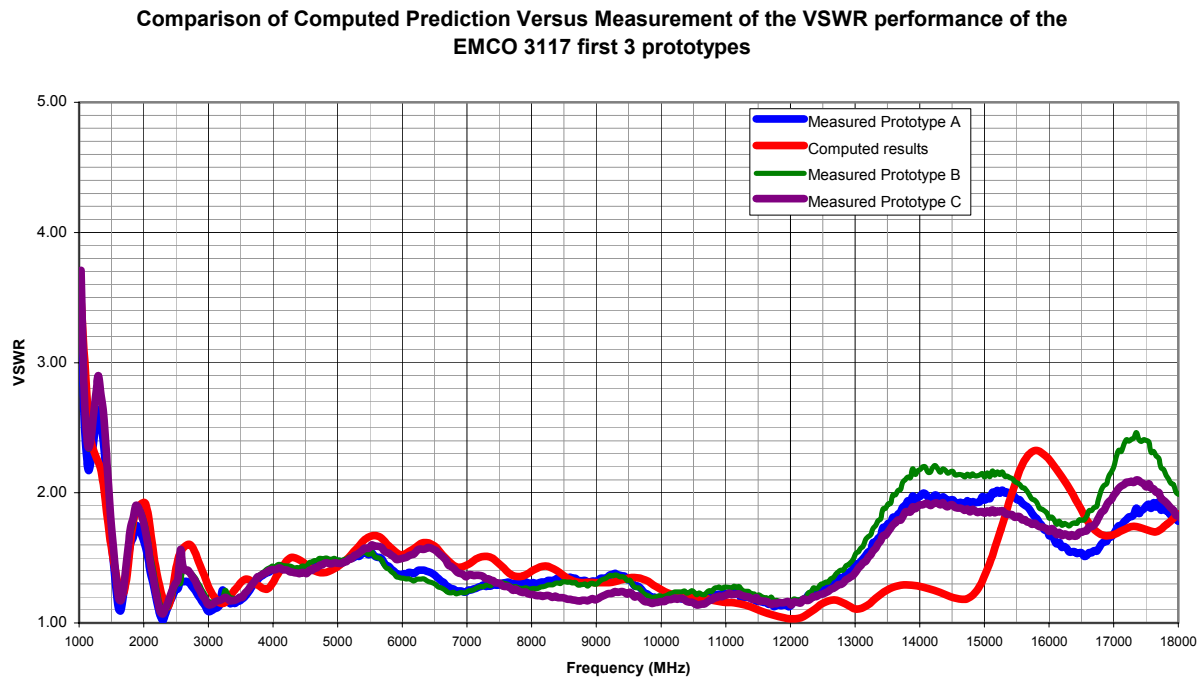


Figure 6. The predicted VSWR compared with the 3 prototype antennas.

The results show very good correlation between model and measurement only at frequencies above 13GHz there is a deviation. This is probably due to not having enough unknowns at the higher end. Due to memory constrains on the model 10 cells per wavelength was the maximum allowed at the highest frequency of interest.

The Gain was measured following the SAE ARP-958-C [4]. Figure 7 shows the comparison between measurement and prediction.

Gain Comparison of three EMCO 3117 prototypes

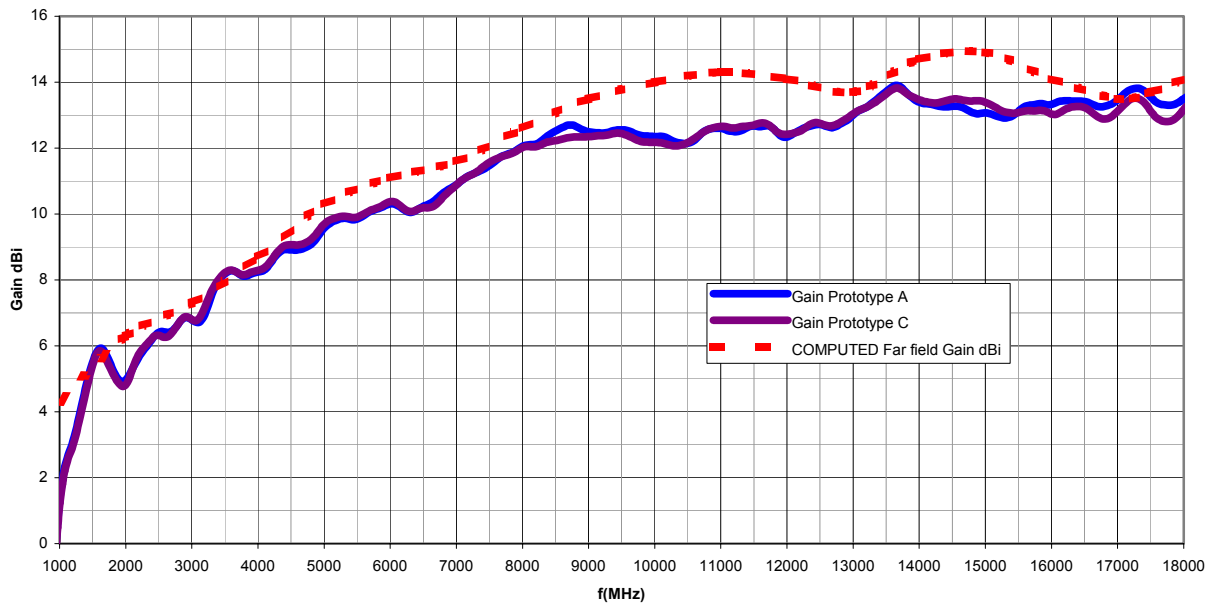


Figure 7. Comparison of directive gain between prototypes and prediction.

Again there is a very good correlation between model and actual measurement. The higher gain of the prediction can be explained by the losses in the aluminum body of the antenna and also effects due to small gaps between the parts that make up the antenna additionally the directivity value provided by the modeling software package was a far field value, while the antenna was measured at 1m distance following the SAE ARP 958 procedure, so some near field gain compression is expected.

The radiation pattern was computed at frequencies every 1GHz between 1 and 18GHz. Additional frequency steps were computed at 18.5 and 19GHz and every .25GHz between 16GHz and 18GHz. Full three-dimensional patterns were measured in an anechoic chamber. Figure 8 shows the two principal planes of the pattern at 10GHz both computed and measured.

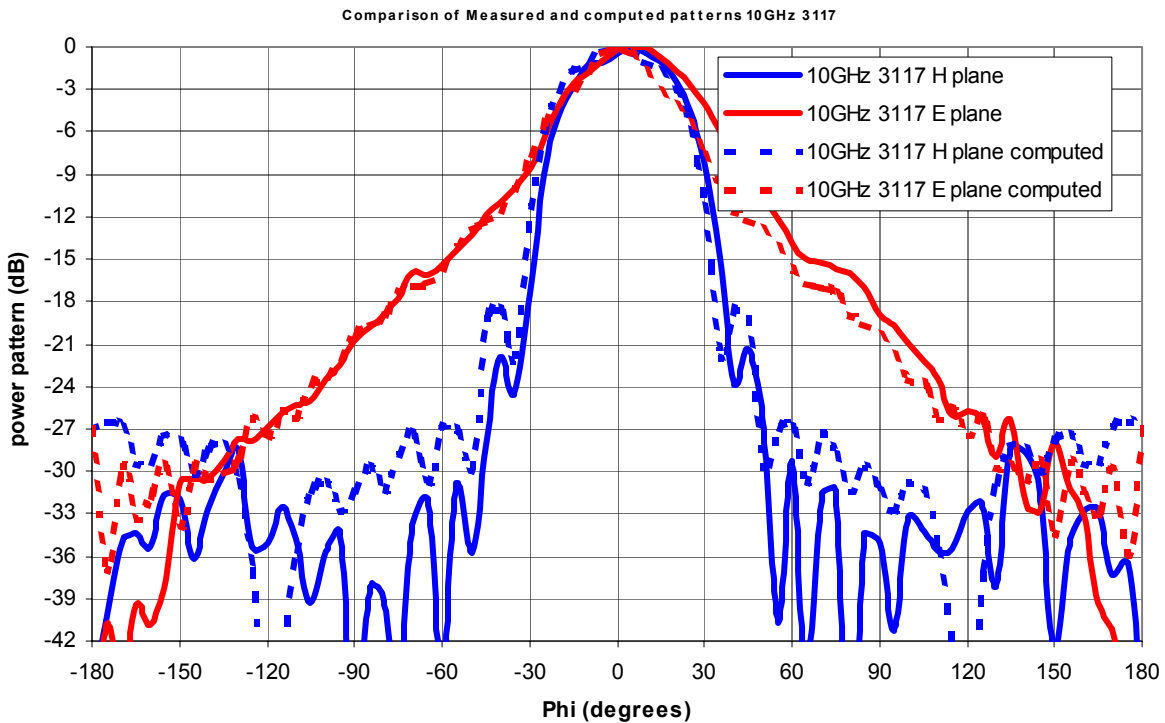


Figure 8. Radiation pattern at the two principal planes at 10GHz. computed and measured.

Figure 8 shows very good agreement between the predicted pattern and the measured results there is a slight shift in the pattern but it is smaller than 5degrees.

Figures 9, 10 and 11 show 3d patterns computed and measured at 16,17 and18GHz, although at 17GHz incipient lobes at  $45^\circ$  appear they never materialized in to four separate beams. Further analysis of the data shows a 1dB ripple maximum in the front end of the main beam.

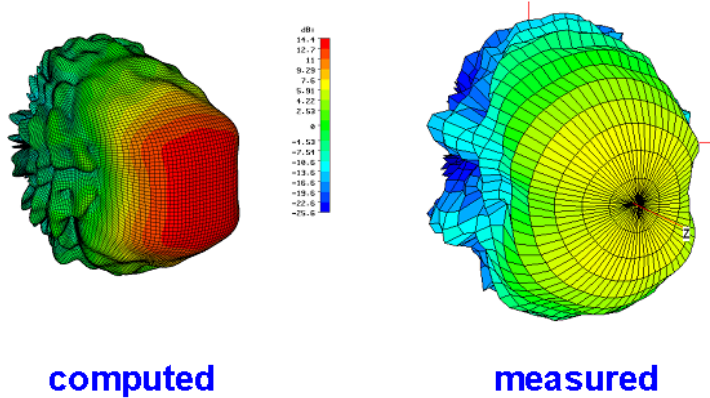


Figure 9. 3D radiation pattern at 16GHz.

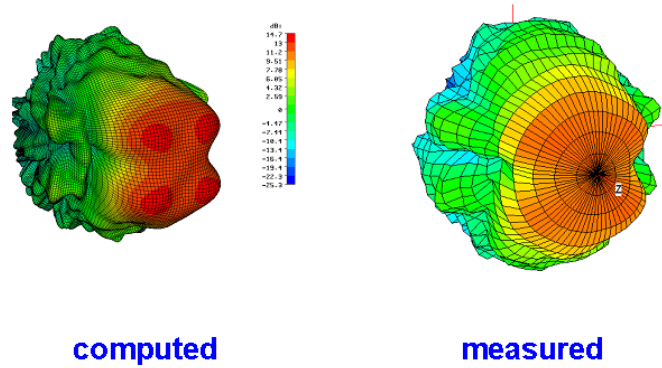


Figure 10. 3D radiation pattern at 17GHz.

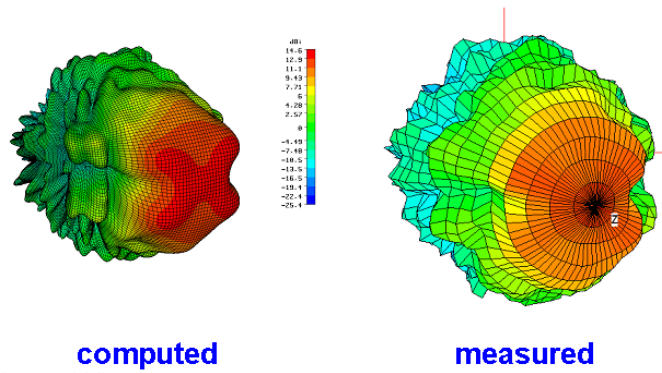
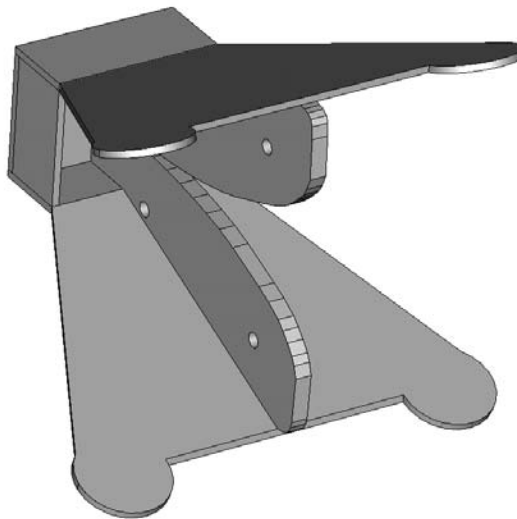


Figure 11. 3D radiation pattern at 18GHz.

Figures 9 to 11 suggest very good correlation between the numerical results and the prototype whose pattern was measured. Further numerical analysis was performed to analyze the possibility of shaping the top and bottom plates for aesthetic and practical reasons. The model in figure 12 showed that there was no mayor effect from extending the top and bottom plates.



Layer type = PEC

Figure 12. Additional model showing the extended corners.

Extending the corners allowed for the horn to be stored facing down. A common practice in EMC laboratories Figure 13 shows the horn stored in this fashion.



Figure 13. The new horn in showing the extended top and bottom that allows for storing it facing down.

#### IV. Comparison with traditional DRGH antenna

As it can be seen from figure 14 the gain from 1GHz to 3GHz is much lower for the new design than for the traditional. However, one must recall that at those frequencies it is still possible to find good power to price ratios for amplifiers. Additionally, note that from 8GHz to 18GHz the gain for the new design is fairly flat with no more than 2dB of variation. That is the range where the advantages of the new design over the traditional are clearly seen.

It is true that the traditional appears to have higher gain from 15 to 16.5GHz, but that corresponds to such a narrow beam that the antenna is useless when it comes to illuminate the equipment under test (EUT). at 18GHz the notch in the traditional design pattern causes the gain to drop about 6dB below the new design gain values.

While it is understood that amplifier power is an issue for EMC engineers. It must be pointed to them the ability of this antenna to generate fairly uniform field planes throughout the frequency range of the antenna. Also, since a wider beam is obtained at 1GHz it is possible to bring the antenna closer to the EUT and still illuminate the entire object with the required field.

Radiation pattern is the key issue on the new design. It has a superior pattern behavior than the traditional horn. Overall the EMC engineer must realize the advantage of having a good pattern behavior for the whole band even if the cost is lower gain for 12% of the operational band of the antenna. Figure 15 shows the measured pattern for the new horn design at 16GHz, it is clear that a smoother and nicer pattern is radiated by the new horn than by the traditional design

## V. Conclusions

The results both measured and predicted show that the new design is comparable in gain and antenna factor (AF) to the traditional horn. The lack of side structures has decreased the low-end gain when compared with the traditional design. Also the open sides have caused the beam-width to be larger at the low end than

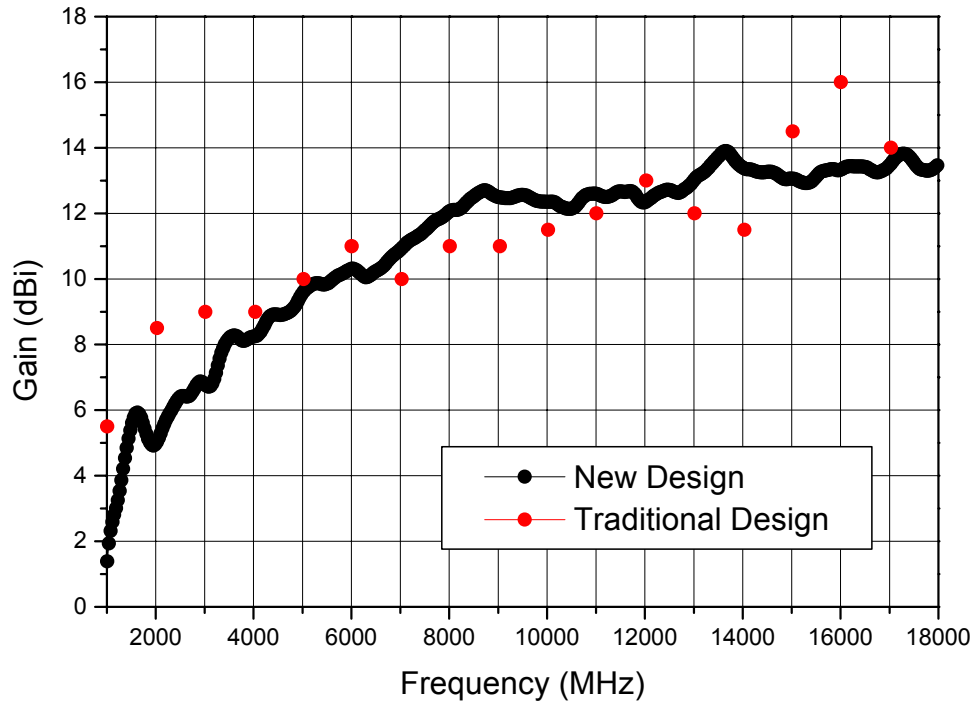


Figure 14. comparison of traditional and new design

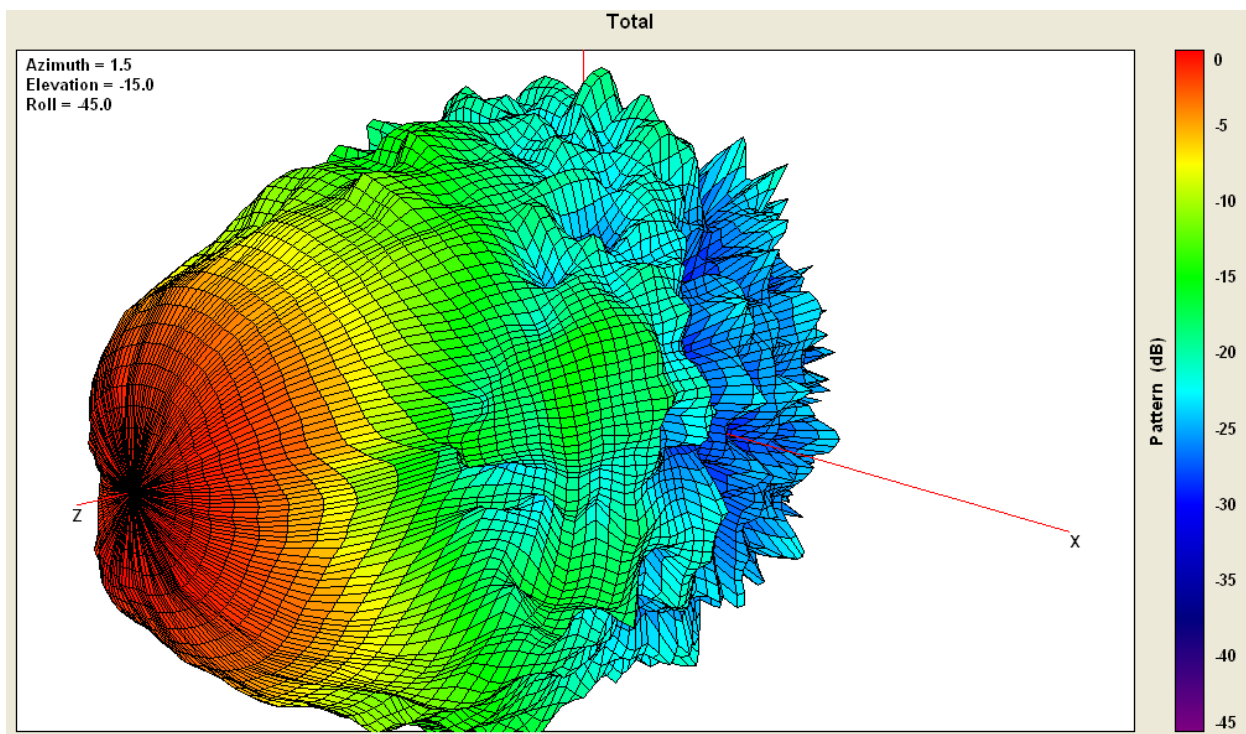


Figure 15. Measured radiation pattern of the new horn design at 16GHz.

the traditional design. However for most of the 1 to 18GHz band the performance is similar and the better pattern behavior has translated in to a more stable gain and AF for the high end of operation. Even more important is that the new design has a better pattern. The main beam does not split in to four separate lobes at any frequency of operation. The result is an antenna that is better suited than the traditional design for EMC applications.

## VI. References

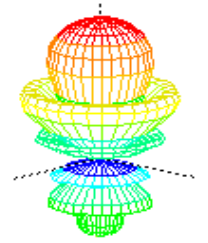
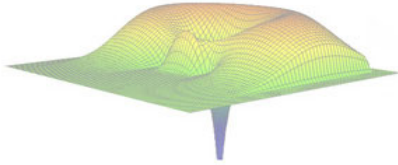
- [1] D Morgan, *A Handbook for EMC testing and Measurement*. Peter Peregrinus Ltd (on behalf of the IEE): London, UK 1994.
- [2] MIL-STD-461-E "Requirements for the Control of Electromagnetic Interference Characteristics of Subsystems and Equipment" Department Of Defense, August 1999.
- [3] C burns, P. Leuchtmann, R. Vahldieck, "Analysis and Simulation of a 1-18GHz Broadband Double-Ridge Horn Antenna", *IEEE Transactions on Electromagnetic Compatibility*, Vol 45, No 1, pp55-60, Feb 2003.
- [4] Society of Automotive Engineers (SAE) *Surface Vehicle Electromagnetic Compatibility (EMC) Standards Manual*. Society of Automotive Engineers, Inc: Warrendale, PA, 1999.



Vicente Rodríguez-Pereyra. Attended the University of Mississippi where he obtained his B.S.E.E. in 1994. During the fall of 1994 he joined the Department of Electrical Engineering at the University of Mississippi as a research assistant. He was involved in projects regarding reduction of cross-talk in high speed digital circuits as part of an Army Research Office grant and on the use of the Finite Difference Time Domain technique in antenna analysis. During this period he completed his Master of Science and Doctorate in the area of Engineering Science with emphasis on Electromagnetic Theory in 1996 and 1999, respectively. On August 1999 Dr. Rodríguez joined the department of Electrical Engineering and Computer Science at Texas A&M University-Kingsville (Formerly Texas A&I University) as a Visiting Assistant Professor. In June 2000 Dr. Rodríguez left the academic world when he joined EMC Test Systems (now ETS-Lindgren) as an RF and Electromagnetics

engineer. During this time he was involved in the anechoic design of several chambers, including rectangular and taper antenna pattern measurement chambers. He was also the principal RF engineer for the anechoic chamber at the Brazilian Institute for Space Research (INPE) the largest chamber in Latin America and the only fully automotive EMC and Satellite testing chamber. In September 2004 Dr. Rodríguez took over the position of Senior Principal Antenna Design Engineer, placing him in charge of the development of new antennas for different applications and on improving the existing antenna line. Among the antennas developed by Dr. Rodriguez are new broadband double ridge guide horns with single lobe pattern and high field generator horns for the automotive industry.

Dr. Rodríguez's interests are Numerical Methods in Electromagnetics and specially when applied to antenna design and analysis, since his association with ETS-Lindgren Dr. Rodríguez's interest has spread to the use of these numerical techniques is designing EMC and RF/MW absorber. Dr. Rodríguez is the author of more than twenty publications including journal and conference papers as well as book chapters. Dr. Rodriguez holds a patent for hybrid absorber design additionally he has a patent pending for a new dual ridge horn antenna design for EMC applications. Dr. Rodríguez is a member of the IEEE and several of its technical societies including the MTT and the EMC societies. Dr. Rodríguez is an active member of the Applied Computational Electromagnetic Society (ACES). He is an Associate Editor of the ACES Journal and chair of the member communications committee of ACES. Dr. Rodriguez has served as a reviewer for the ACES Journal and for the Journal of Electromagnetic Waves and Applications. He has co-chaired a session during the 2003 ACES symposium and workshops during the 2002 and 2004 IEEE, EMC annual symposiums. Dr. Rodríguez is a Full member of the Sigma Xi Scientific Research Society and of the Eta Kappa Nu Honor Society.



# ACES

## Applied Computational Electromagnetic Society

ACES Web Site: <http://aces.ee.olemiss.edu>

### CALL FOR PAPERS

**The 22<sup>nd</sup> International Review of Progress in Applied Computational Electromagnetics (ACES 2006)**  
**March 12 - 16, 2006**  
**Hyatt Regency Miami, Miami, Florida**

The purpose of the international annual ACES Symposium is to bring developers, analysts, and users together to share information and experience about the practical application of EM analysis using computational methods. The symposium offers technical presentations, demonstrations, vendor booths, short courses, and hands-on workshops. The technical program will be organized in two parallel sessions with 30-minute oral presentations in the mornings and afternoons along with three poster sessions. All aspects of electromagnetic computational analysis are represented.

The ACES Symposium is a highly influential outlet for promoting awareness of recent technical contributions to the advancement of computational electromagnetics. Attendance and professional program paper participation from non-ACES members and from outside North America are encouraged and welcome.

Papers may address general issues in applied computational electromagnetics or may focus on specific applications, techniques, codes, or computational issues of potential interest to the Applied Computational Electromagnetics Society membership. The following is a list of suggested topics, although contributions in other areas of computational electromagnetics are encouraged and will be considered.

#### Suggested Topics:

Integral Equation Methods	Smart Antenna and Arrays
Differential Equation Methods	EBG and Artificial Materials
Fast and Efficient Methods	Frequency Selective Surfaces
Hybrid Techniques	MEMS- NEMS and MMIC
Inverse Scattering Techniques	EMC/EMI
Optimization Techniques for CEM	Propagation
Asymptotic and High Frequency Techniques	Remote Sensing
Low Frequency Electromagnetics	RF and Microwave Devices
Computational Bio-Electromagnetics	Pre- and Post-processing
Printed and Conformal Antennas	NEC Modeling and Analysis
Wideband and Multiband Antennas	FEKO Modeling and Analysis
Dielectric Resonator Antennas	WIPL-D Modeling and Analysis
Phased Array Antennas	

All authors of accepted papers will have the option to submit an extended version of their paper or papers for review and publication in a special issue of the ACES Journal.

## SYMPOSIUM STRUCTURE

The international annual ACES Symposium traditionally takes place during one week of March annually, and includes: (1) oral-invited sessions, (2) poster sessions, (3) a student paper competition, (4) short courses, (5) an awards banquet, (6) vendor exhibits, and (7) social events. The ACES Symposium also includes plenary and panel sessions, where invited speakers deliver original essay-like reviews of hot topics of interest to the computational electromagnetics community.

## PAPER FORMATTING REQUIREMENTS

The recommended paper length, including text, figures, tables and references, is four (4) pages, with eight (8) pages as a maximum. Submitted papers should be formatted for printing on 8.5x11-inch U.S. standard paper, with 1-inch top, bottom, and side margins. On the first page, the title should be 1-1/2 inches from top with authors, affiliations, and e-mail addresses beneath the title. Use single line spacing, with 11 or 12-point font size. The entire text should be fully justified (flush left and flush right). No typed page numbers. A sample paper can be found in the conference section on ACES web site at: <http://aces.ee.olemiss.edu>. Each paper should be submitted in camera-ready format with good resolution and clearly readable.

## PAPER SUBMISSION PROCEDURE

**No email, fax or hard-copy paper submission will be accepted.** Photo-ready finished papers are required, in Adobe Acrobat format (\*.PDF) and must be submitted through ACES web site using the "Upload" button in the left menu, followed by the selection of the "Conference" option, and then following the on-line submission instructions. Successful submission will be acknowledged automatically by email after completing all uploading procedure as specified on ACES web site.

## SUBMISSION DEADLINE AND REGISTRATION REQUIREMENT

Submission deadline is **December 15, 2005**. A signed ACES copyright-transfer form must be mailed to the conference technical chair immediately following the submission as instructed in the acknowledgment of submission email message. Papers without an executed copyright form will not be considered for review and possible presentation at the conference. Upon the completion of the review process, by the technical program committee, the acceptance notification along with the pre-registration information will be mailed to the corresponding author on or about **January 15, 2006**. Each presenting author is required to complete the paid pre-registration and the execution of any required paper corrections by the firm deadline of **January 30, 2006** for final acceptance for presentation and inclusion of accepted paper in the symposium proceedings.

## BEST STUDENT PAPERS CONTEST

The best three (3) student papers presented at the 22<sup>nd</sup> Annual Review will be announced at the symposium banquet. Members of the ACES Board of Directors will judge student papers submitted for this competition. The first, second, and third winners will be awarded cash prizes of **\$300, \$200, and \$100**, respectively.

For any questions please contact the conference secretary: **Ms. Dora Hernadez** (305) 348-3701, [hernandd@fiu.edu](mailto:hernandd@fiu.edu), or visit ACES on-line at: <http://aces.ee.olemiss.edu>

<b>General Chair</b>	<b>Technical Program Chair</b>	<b>Short Course Chair</b>	<b>Exhibits Chair</b>	<b>Publicity Chair</b>
<i>Osama Mohammed</i>	<i>Atef Elsherbeni</i>	<i>Alexander Yakovlev</i>	<i>Andrew L. Drozd</i>	<i>C. J. Reddy</i>
Florida International University	The University of Mississippi	The University of Mississippi	ANDRO Consulting	EM Software & Systems

<b>ADVERTISING RATES</b>		
	<b>FEE</b>	<b>PRINTED SIZE</b>
Full page	\$200	7.5" × 10.0"
1/2 page	\$100	7.5" × 4.7" or 3.5" × 10.0"
1/4 page	\$50	3.5" × 4.7"
<p>All ads must be camera ready copy.</p> <p>Ad deadlines are same as Newsletter copy deadlines.</p> <p>Place ads with Ray Perez, Newsletter Editor, Martin Marietta Astronautics, MS 58700, PO Box 179, Denver, CO 80201, USA. The editor reserves the right to reject ads.</p>		

<b>DEADLINE FOR THE SUBMISSION OF ARTICLES</b>	
<b>Issue</b>	<b>Copy Deadline</b>
March	February 1
July	June 1
November	October 1

For the **ACES NEWSLETTER**, send copy to Bruce Archambeault in the following formats:

1. A PDF copy.
2. A MS Word (ver. 97 or higher) copy. If any software other than WORD has been used, contact the Managing Editor, Richard W. Adler **before** submitting a diskette, CD-R or electronic file.

### **Last Word**

“Make everything as simple as possible, but not simpler“  
Albert Einstein